Article

Electro-generated excitons for tunable lanthanide electroluminescence

https://doi.org/10.1038/s41586-025-09717-1

Received: 12 January 2025

Accepted: 7 October 2025

Published online: 19 November 2025

Open access

Check for updates

Jing Tan[1,8], Peng Zhang[2,8], Xiaoqing Song[1,8], Chunmiao Han[1]✉, Feng Wang[3], Jing Zhang[1], Chunbo Duan[1], Zhilong Zhang[4], Sanyang Han[2]✉, Hui Xu[1]✉ & Xiaogang Liu[5,6,7]✉

Lanthanide nanocrystals offer unique advantages for electroluminescence (EL) applications, including narrow-band emission, high colour purity and compositionally tunable output[1–4]. However, their insulating nature poses a challenge for carrier transport and injection, impeding their application in electrically driven optoelectronic devices[5]. Here we demonstrate efficient EL from insulating lanthanide fluoride nanocrystals (4 nm; $NaGdF_4$:X; X = Tb^{3+}, Eu^{3+} or Nd^{3+}) coated with a series of functionalized 2-(diphenylphosphoryl)benzoic acids (ArPPOA). These ligands, featuring donor–phosphine oxide acceptor hybrids with carboxyl and P=O coordination sites, effectively sensitize the luminescence of lanthanide nanocrystals by modulating the intraligand charge transfer characteristics. Ultrafast spectroscopic investigations reveal that strong coupling between ArPPOA and lanthanide nanocrystals facilitates intersystem crossing (ISC; <1 ns) and highly efficient triplet energy transfer to nanocrystals (up to 96.7%). Through careful control of dopant composition and concentration in nanocrystals, we also achieve wide-ranging multicolour EL without altering the device architecture, reaching an external quantum efficiency exceeding 5.9% for Tb^{3+}. This ligand-functionalized nanocrystal platform provides a modular strategy for exciton control in insulating nanocrystal systems, offering a pathway for spectrally precise electroluminescent materials.

EL, which enables the direct conversion of electrical energy into light, is important for a wide range of optoelectronic applications, including displays, sensors, healthcare diagnostics, quantum information systems, neuromorphic computing and wearable devices[6–14]. Across these applications, there is growing demand for electroluminescent materials that combine high spectral precision, multicolour tunability and robust operational stability, ideally within simplified and scalable device architectures[15–17]. Despite considerable progress in organic emitters, quantum dots and hybrid perovskites, conventional electroluminescent systems continue to face limitations, particularly in exciton management, colour fidelity under electrical bias and the need for wavelength-specific emission layers that often require complex, multilayer charge-injection structures[18,19].

Lanthanide-doped nanocrystals offer a fundamentally distinct approach to EL engineering. Their atomically defined 4f–4f transitions yield narrow emission lines (<10 nm full width at half maximum)[2,20], exceptional photochemical and thermal stability[21–23], long excited-state lifetimes (on the millisecond scale)[24,25] and defect-insensitive emission[26], all of which are advantageous for spectrally precise and stable EL operation. Also, their composition-dependent tunability allows for integration of multicolour emission within a shared materials framework[27,28]. However, these advantages come with substantial challenges. Lanthanide-doped matrices such as $NaLnF_4$ are electrically insulating and direct carrier injection into 4f orbitals is inefficient owing to their localized nature[5]. These limitations have so far hindered the development of lanthanide-based electroluminescent systems and left fundamental questions about exciton generation, transport and energy transfer in these hybrids largely unexplored.

Here we introduce a molecularly engineered lanthanide nanohybrid platform that overcomes key barriers to efficient EL by decoupling charge transport from photon emission[29–31]. Specifically, we functionalize fluoride-based lanthanide nanocrystals ($NaGdF_4$:X, in which X = Tb^{3+}, Eu^{3+} or Nd^{3+}) with rationally designed carbazole–phosphine oxide ligands (for example, CzPPOA) that acts as both charge-transport media and exciton harvesters. These ligands form a soft electronic interface that enables fast, directional energy transfer to localized 4f states, thus activating electrically triggered lanthanide emission without the need for dedicated carrier-injection layers. We systematically investigate the EL mechanisms in these nanohybrids, including interfacial exciton transfer dynamics, ligand design principles and multicolour output from a unified device structure.

As a proof of concept, we synthesized 4-nm $NaGdF_4$:Tb nanocrystals functionalized with five aryl phosphine oxide carboxylic acid (ArPPOA) ligands featuring different substitution groups: H (TPPOA),

[1]Key Laboratory of Functional Inorganic Material Chemistry (Ministry of Education) & School of Chemistry and Material Science, Heilongjiang University, Harbin, China. [2]Institute of Biopharmaceutical and Health Engineering, Shenzhen International Graduate School, Tsinghua University, Shenzhen, China. [3]Department of Materials Science and Engineering, City University of Hong Kong, Kowloon, Hong Kong SAR, China. [4]South China Advanced Institute for Soft Matter Science and Technology, School of Emergent Soft Matter, South China University of Technology, Guangzhou, China. [5]Department of Chemistry, National University of Singapore, Singapore, Singapore. [6]Department of Materials Science and Engineering, National University of Singapore, Singapore, Singapore. [7]Center for Functional Materials, National University of Singapore Suzhou Research Institute, Suzhou, China. [8]These authors contributed equally: Jing Tan, Peng Zhang, Xiaoqing Song. ✉e-mail: hanchunmiao@hlju.edu.cn; hansanyang@sz.tsinghua.edu.cn; hxu@hlju.edu.cn; chmlx@nus.edu.sg

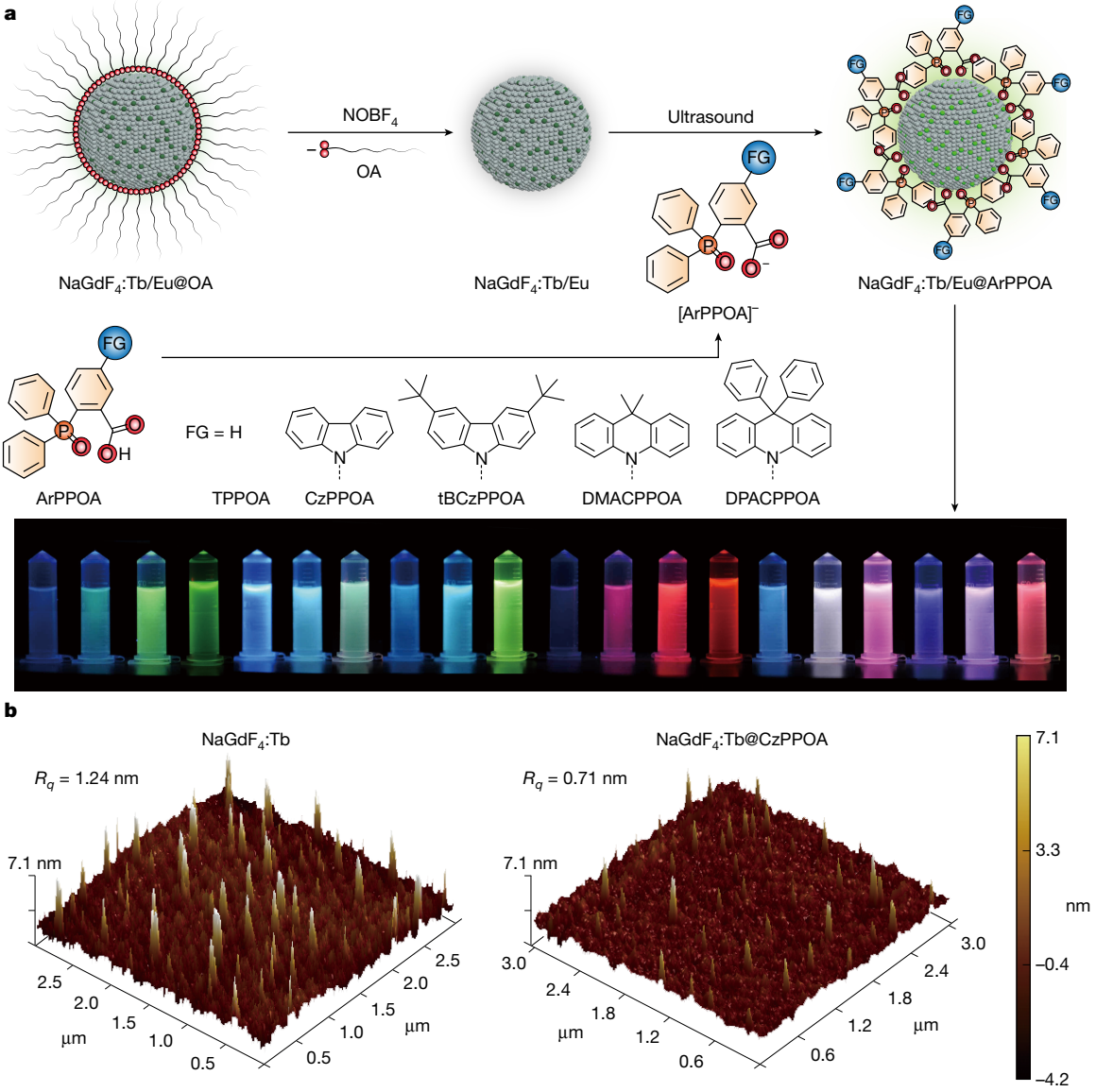

Fig. 1 | System design of phosphine oxide–lanthanide fluoride nanocrystal emitters. a, Schematic of the synthetic procedure for 4-nm $NaGdF_4$:Tb/Eu nanocrystals capped with ArPPOA ligands. FG refers to functional groups used to modify the ArPPOA ligands. The bottom panel shows photographs of multicolour emissions from $NaGdF_4$:Tb/Eu@ArPPOA dispersed in ethanol (1 mg ml^{-1}) excited with a 365-nm ultraviolet lamp, demonstrating the tunable emission colours achieved by varying the dopant composition. **b**, Atomic force microscopy images of spin-coated films made from ligand-free $NaGd_{0.6}F_4$:$Tb_{0.4}$ nanocrystals and $NaGd_{0.6}F_4$:$Tb_{0.4}$@CzPPOA nanohybrids. The root-mean-square roughness (R_q) values are provided to illustrate the improved film formability and surface smoothness achieved with the ligand-functionalized nanocrystals compared with the ligand-free counterparts.

carbazole (CzPPOA), 3,6-di(*tert*-butyl)carbazole (tBCzPPOA), 9,9-dimethylacridine (DMACPPOA) and 9,9-diphenylacridine (DPACPPOA) (Fig. 1a, Extended Data Fig. 1 and Supplementary Fig. 1). The conjugation of nanocrystals with these organic semiconducting ligands effectively passivates surface defects and sensitizes the nanocrystals, enhancing luminescence efficiency. The molecular design incorporates electron-donating groups to adjust the energy levels of frontier molecular orbitals and excited states. By varying donor groups such as Cz, tBCz, DMAC and DPAC, the intramolecular charge transfer interactions between donors and the diphenylphosphine oxide (DPPO) acceptor can be tuned to regulate the excited-state characteristics of ligands. The nanohybrids, $NaGdF_4$:Tb@ArPPOA, were prepared using a two-step ligand exchange process, resulting in nanocrystals well dispersed in ethanol. Compared with their ligand-free counterparts, $NaGdF_4$:Tb@CzPPOA spin-coated films exhibit much improved film formability (Fig. 1b).

The ArPPOA ligands predominantly contribute to the electronic absorption spectra of $NaGdF_4$:Tb@ArPPOA in dilute ethanol solutions (2 mg ml^{-1}) and films, corresponding to the $\pi \rightarrow \pi^*$ and $n \rightarrow \pi^*$ transitions of the donors and DPPO groups, respectively (Extended Data Fig. 2 and Supplementary Table 1). These absorption characteristics align with those of the corresponding complexes (Supplementary Fig. 2 and Supplementary Table 2). Photoluminescence (PL) investigations revealed that ligand modification greatly enhances the intensity of Tb^{3+} emission ($^5D_4 \rightarrow {}^7F_j$ transitions, $j = 3–6$) compared with ligand-free nanocrystals, which can be attributed to the efficient sensitization effect (Supplementary Figs. 3 and 4). For Eu^{3+}-doped nanocrystals, ligand-associated emission bands become more pronounced, yielding pink and even white emission colours (Fig. 1a, bottom panel).

The emission intensity of $NaGdF_4$:Tb@ArPPOA films strongly depends on the concentration of emissive Tb^{3+} dopants and the surface ligand density on nanocrystals. Increasing the Tb^{3+} concentration

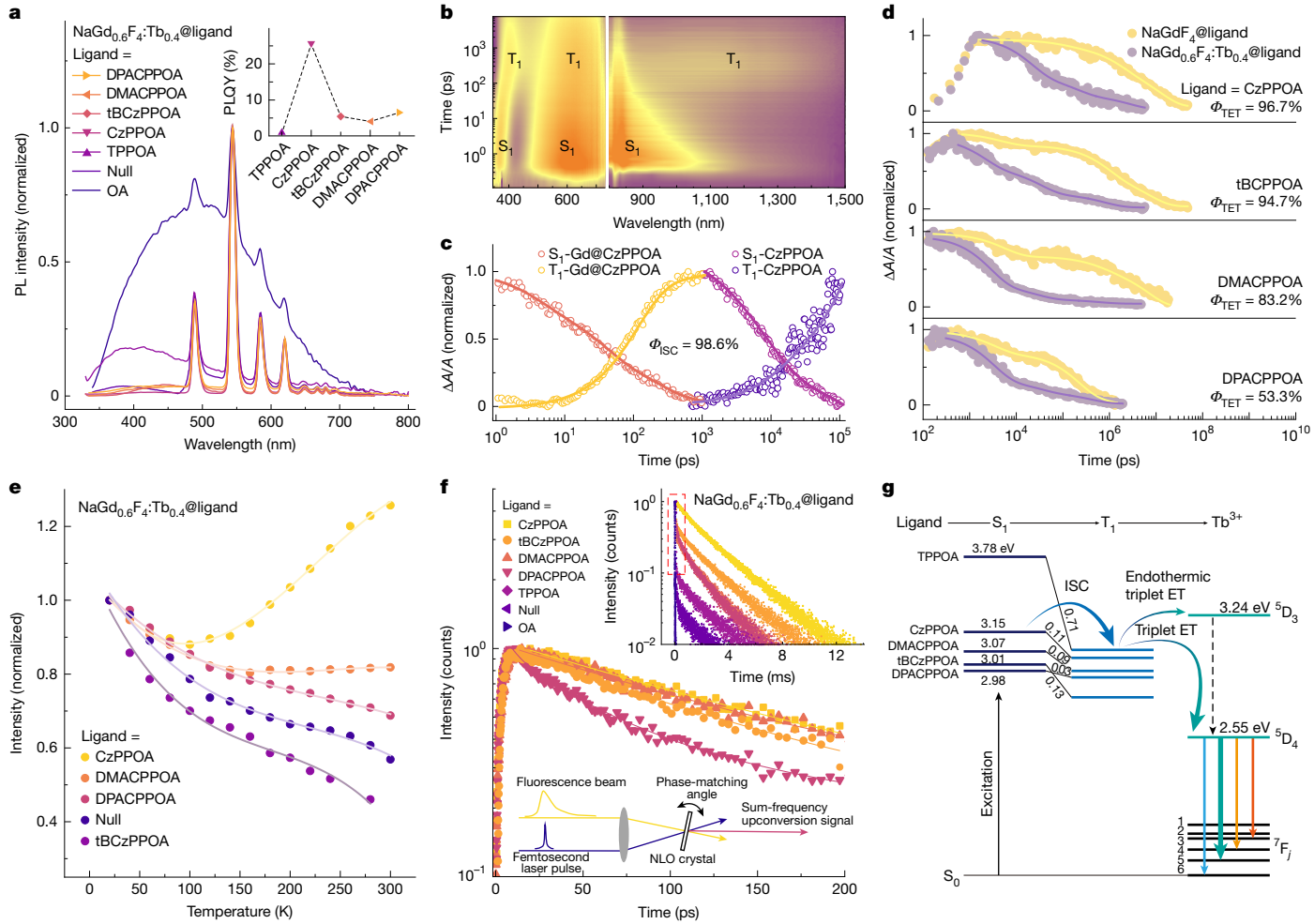

Fig. 2 | Photophysical properties of $NaGd_{1-x}F_4:Tb_x$@ArPPOA nanohybrids. **a**, PL spectra and corresponding PLQYs (inset) of spin-coated $NaGd_{0.6}F_4:Tb_{0.4}$@ArPPOA films. For comparison, spectra of OA-capped ($NaGd_{0.6}F_4:Tb_{0.4}$@OA) and ligand-free ($NaGd_{0.6}F_4:Tb_{0.4}$) samples are also shown. **b**, Two-dimensional pseudo-colour transient absorption spectrum of $NaGdF_4$@CzPPOA (345-nm pump; 7-ns time window). **c**, Extracted singlet (S_1) decay and triplet (T_1) formation kinetics of CzPPOA in pristine form and when bound to $NaGdF_4$. Coordination shortens the singlet lifetime from 60.9 ns to 874.6 ps, indicating enhanced ISC. **d**, Triplet-state decay kinetics of ArPPOA on $NaGdF_4$ and $NaGd_{0.6}F_4:Tb_{0.4}$, confirming efficient energy transfer to Tb^{3+}. **e**, Temperature-dependent integrated PL intensity of $NaGd_{0.6}F_4:Tb_{0.4}$@ArPPOA, revealing phonon-assisted luminescence enhancement. **f**, Femtosecond sum-frequency upconversion signal decay profiles of $NaGd_{0.6}F_4:Tb_{0.4}$@ArPPOA at 547 nm (temporal resolution: 250 fs). Inset, time-resolved PL decay at the same wavelength (temporal resolution: 1.8 μs). **g**, Energy-level diagram of $NaGd_{0.6}F_4:Tb_{0.4}$@ArPPOA illustrating the energy-transfer mechanism. S_0, S_1 and T_1 denote the ground, first singlet and first triplet states, respectively. ET, energy transfer; NLO, nonlinear optics; TET, triplet energy transfer.

enhances the trapping of excitation energy from surface-excited ligands. However, excessive concentrations of Tb^{3+} emitters can lead to detrimental cross-relaxation effects. By carefully optimizing the dopant concentration, we identified 40% Tb^{3+} doping as the optimal level, yielding maximum emission intensity in $NaGdF_4$:Tb@CzPPOA films (Supplementary Fig. 5). In parallel, ultraviolet–visible absorption analysis revealed that the surface of each nanocrystal is coated with CzPPOA ligands at an average density of one molecule per 2.9 nm^2, indicating a well-dispersed and tightly packed ligand shell (Supplementary Fig. 6).

Donor-modified $NaGdF_4$:Tb@ArPPOA films exhibited strong Tb^{3+} emission with negligible ligand emission. By contrast, unmodified $NaGdF_4$:Tb@OA and $NaGdF_4$:Tb@TPPOA films showed distinct ligand emission bands (400–600 nm), attributed to oleic acid (OA) and TPPOA, respectively (Fig. 2a). Notably, the photoluminescence quantum yield (PLQY) of $NaGd_{0.6}F_4:Tb_{0.4}$@ArPPOA films increased by several orders of magnitude compared with ligand-free counterparts (Fig. 2a inset). By fine-tuning the donor group within the ligands, a PLQY of 25.55 ± 1.58% and 44.29 ± 0.93% was achieved in $NaGd_{0.6}F_4:Tb_{0.4}$@CzPPOA films and in solution, respectively (Supplementary Fig. 7 and Supplementary Tables 1 and 3).

To further investigate the interfacial energy-transfer mechanism, we measured the fluorescence and phosphorescence spectra of sodium carboxylate analogues to determine ligand singlet (S_1) and triplet (T_1) energy levels (Supplementary Figs. 8 and 9 and Supplementary Table 3). The large energy gaps between the S_1 or T_1 states of TPPOA and the Tb^{3+} emitting level ($^5D_4$) were calculated to be 1.23 or 0.52 eV, respectively, resulting in inefficient energy transfer. By contrast, electron donor substitution lowered both the energy levels and singlet–triplet splitting ($\Delta E_{S\text{-}T}$), reducing the energy mismatch with Tb^{3+} and enhancing transfer efficiency (Supplementary Table 3). Transient absorption spectroscopy of $NaGdF_4$@CzPPOA revealed initial photoinduced absorption from the S_1 state (350–1,100 nm) (Fig. 2b and Extended Data Fig. 3), followed by T_1 state photoinduced absorption features (400–700 nm and 900–1,500 nm). Kinetic analysis revealed that coordination with lanthanide ions accelerates ISC to the sub-nanosecond process range, enabled by the small $\Delta E_{S\text{-}T}$ and spin-exchange coupling with 4f electrons[30] (Fig. 2c). This ISC process reaches a conversion efficiency of

98.6% (Supplementary Figs. 10–18, Extended Data Fig. 4 and Supplementary Table 3), indicating that Tb^{3+} emission is dominantly sensitized by molecular T_1 state.

We further investigated T_1 dynamics across samples. The T_1 lifetime substantially decreased on Tb^{3+} coordination (Fig. 2d), indicating efficient ligand-to-ion triplet energy transfer. The tBCzPPOA ligand, with the smallest T_1–$^5D_4$ gap (0.33 eV), showed 94.7% energy transfer efficiency (Supplementary Figs. 19–23 and Supplementary Table 3). Despite a large T_1–$^5D_4$ gap (0.49 eV), $NaGd_{0.6}F_4$:$Tb_{0.4}$@CzPPOA films achieved near-unity triplet transfer (96.7%) and the highest PLQY observed. Temperature-dependent PL measurements showed enhanced Tb^{3+} emission from 100 to 300 K, suggesting endothermic energy transfer from the ligand T_1 to the Tb^{3+} $^5D_3$ state (Fig. 2e and Supplementary Fig. 24). Femtosecond sum-frequency upconversion spectroscopy revealed that fluorescence lifetime shortening in $NaGd_{0.6}F_4$:$Tb_{0.4}$@ArPPOA nanohybrids correlates with increased ligand vibrational modes (Fig. 2f), indicating vibrationally mediated fluorescence quenching. Ligand modification also prolonged the 547-nm emission lifetime by three orders of magnitude compared with ligand-free nanocrystals, indicating effective surface passivation and enhanced energy transfer (Fig. 2f inset and Supplementary Figs. 25–29). By contrast, the rigid CzPPOA ligand suppressed non-radiative decay, facilitating efficient sensitization of Tb^{3+} excited states. Among the ArPPOA variants tested, CzPPOA exhibited the highest sensitization efficiency for Tb^{3+}-doped nanocrystals (Fig. 2g).

We investigated the electrical properties of the $NaGdF_4$:Tb@ArPPOA nanohybrids using cyclic voltammetry (Supplementary Fig. 30). The results showed that the electrochemical behaviours of the nanohybrids were dominantly contributed by that of the corresponding ligands. The cathodic peaks corresponded to the reduction of DPPO groups, whereas the carbazole and acridine groups determined the oxidation potentials in the anodic curves. Unlike the unipolar TPPOA, donor-functionalized ligands exhibited ambipolar characteristics, addressing the limitations of insulating $NaGdF_4$:Tb and enhancing its electrical performance.

Encouraged by the high PL properties and improved electroactivity of the nanohybrids, we fabricated four-layer-structured light-emitting diode (LED) devices using spin-coated *m*CP:*y*% $NaGd_{0.6}F_4$:$Tb_{0.4}$@ligand (*m*CP = 1,3-bis(carbazol-9-yl)benzene) as the emitting layer (Fig. 3a). The LED based on $NaGd_{0.6}F_4$:$Tb_{0.4}$@CzPPOA exhibited the pure characteristic peaks of Tb^{3+} at 488, 544, 584 and 620 nm, corresponding to Commission Internationale de l'Eclairage (CIE1931) chromaticity coordinates of (0.28, 0.54) (Fig. 3b,c, Extended Data Fig. 5, Supplementary Figs. 31–33 and Supplementary Tables 4 and 5). By contrast, the LED using $NaGd_{0.6}F_4$:$Tb_{0.4}$@OA showed dominant EL from *m*CP, with only weak Tb^{3+} emission detected at high driving voltages. This limitation arises because the OA ligand, lacking optoelectronic activity, hinders carrier and energy transfer from the *m*CP matrix to the electrically inert nanocrystals. Electroactive donor-modified ligands markedly reduced the driving voltages of the devices compared with that of OA-modified nanocrystals. The turn-on voltage for the $NaGd_{0.6}F_4$:$Tb_{0.4}$@CzPPOA-based device was measured to be 4.1 V, comparable with conventional LED devices with conducting emitters (Fig. 3c). Its luminance was approximately 71 times higher than that of the $NaGd_{0.6}F_4$:$Tb_{0.4}$@OA-based device. To evaluate EL stability, control devices using perovskite quantum dots and 2,3,5,6-tetrakis(carbazol-9-yl)-1,4-dicyanobenzene (4CzTPN) were fabricated for comparison (Supplementary Figs. 34 and 35). The suboptimal $NaGd_{0.6}F_4$:$Tb_{0.4}$@CzPPOA-based device demonstrated superior operational lifetime compared with both 4CzTPN-based and perovskite-based analogues under identical device fabrication and testing conditions, highlighting the advantage of ligand-functionalized lanthanide fluoride nanocrystals in achieving stable EL.

The $NaGd_{0.6}F_4$:$Tb_{0.4}$@CzPPOA-based LEDs achieved state-of-the-art performance metrics, including a current efficiency (η_{CE}) of 9.99 cd A^{-1}, power efficiency (η_{PE}) of 7.66 lm W^{-1} and external quantum efficiency (η_{EQE}) of 5.9%. This represents the first demonstration of efficient LEDs based on insulative emitters (Fig. 3d and Supplementary Fig. 36). Compared with $NaGd_{0.6}F_4$:$Tb_{0.4}$@OA and ligand-free $NaGd_{0.6}F_4$:$Tb_{0.4}$ nanocrystals, the η_{EQE} was enhanced by 12-fold and 76-fold, respectively. Considering an outcoupling ratio of 0.25 for indium tin oxide (ITO) glass, the exciton utilization efficiency (η_{EUE}) of $NaGd_{0.6}F_4$:$Tb_{0.4}$@CzPPOA-based devices was calculated to be as high as 88%. These results highlight the dual role of CzPPOA ligands: sensitizing the inorganic cores and facilitating carrier and energy transfer to the nanohybrid emitter during the EL process.

Lifetime measurements showed that $NaGd_{0.6}F_4$:$Tb_{0.4}$@CzPPOA-based devices exhibited the longest EL lifetimes and durations, approximately seven times and an order of magnitude longer than those of ligand-free and OA-capped nanocrystal-based devices, respectively (Fig. 3e and Supplementary Figs. 37 and 38). Notably, the decays in all devices were biexponential, with components on the microsecond (μs) and millisecond (ms) scales. The short and long components of the lifetime were attributed to surface and core Tb^{3+} emitters within $NaGd_{0.6}F_4$:$Tb_{0.4}$@CzPPOA nanocrystals, respectively.

To further verify the critical role of ligands in exciton allocation and energy transfer within nanohybrid-based LED devices, we measured sliced time-resolved electroluminescence emission spectra (TREES) (Fig. 3f and Supplementary Figs. 39 and 40). During the initial 20 μs of carrier recombination in devices using ligand-free and OA-capped nanocrystals, excitons were fully formed and confined within the *m*CP matrix. Consequently, only fluorescence and phosphorescence from *m*CP in the range 350–450 nm were observed, with nanocrystals excluded from exciton utilization. By contrast, in $NaGdF_4$:Tb@CzPPOA-based devices, emissions exclusively from CzPPOA and Tb^{3+} were detected during carrier recombination, indicating rapid host-to-ligand energy transfer and effective exciton confinement on $NaGdF_4$:Tb@CzPPOA.

The ability of the nanocrystals to emit variable colours by simply adjusting dopant composition and concentration offers a straightforward method for colour modulation in LEDs without requiring changes to the device structure. To explore this capability, we prepared 4-nm $NaGd_{0.6}F_4$:$Tb_{0.4-x}Eu_x$@CzPPOA nanocrystals and studied their optical properties (Extended Data Fig. 6). By tuning the concentrations of Tb^{3+} and Eu^{3+} dopants, we achieved continuous emission colour transitions from green to yellow and orange–red (Fig. 4a inset). The emission intensity of Eu^{3+} increased proportionally with its concentration, whereas the Tb^{3+} emission intensity decreased correspondingly (Fig. 4a and Supplementary Figs. 41–44). We further fabricated LED devices using these nanocrystals as emitters. The EL spectrum reveals that the luminescence intensity at 615 nm, the characteristic emission wavelength of Eu^{3+}, substantially enhances with increasing Eu^{3+} content (Fig. 4b). The devices exhibited high-colour-purity EL emissions, ranging from warm white to pure white (Fig. 4c), corresponding to CIE1931 coordinates decreasing from (0.29, 0.46) to (0.38, 0.42), closely matching or equal to illuminants A (0.45, 0.41) and D50 (0.35, 0.36). η_{CE}, η_{PE} and η_{EQE} of the as-prepared $NaGd_{0.6}F_4$:$Tb_{0.39}Eu_{0.01}$@CzPPOA device were measured to be 8.48 cd A^{-1}, 6.34 lm W^{-1} and 5.09%, respectively (Fig. 4d,e and Supplementary Table 6). TREES and decay studies confirmed that exciton allocation in the EL process was consistent with energy transfer observed during the PL process (Supplementary Fig. 45). Compared with white organic LEDs, which rely on complex architectures with several hosts and layers, this ligand-functionalized nanocrystal platform offers a highly versatile and efficient solution for achieving wide-band tunable emissions, eliminating the need for materials or device-structure modifications. We further demonstrated the unique near-infrared luminescence tunability of lanthanide-doped nanocrystals by directly doping Nd^{3+} ions without modifying the device architecture or surface ligands, achieving 1,064-nm emission with conventional near-infrared organic/quantum dot LED technologies (Extended Data Fig. 7).

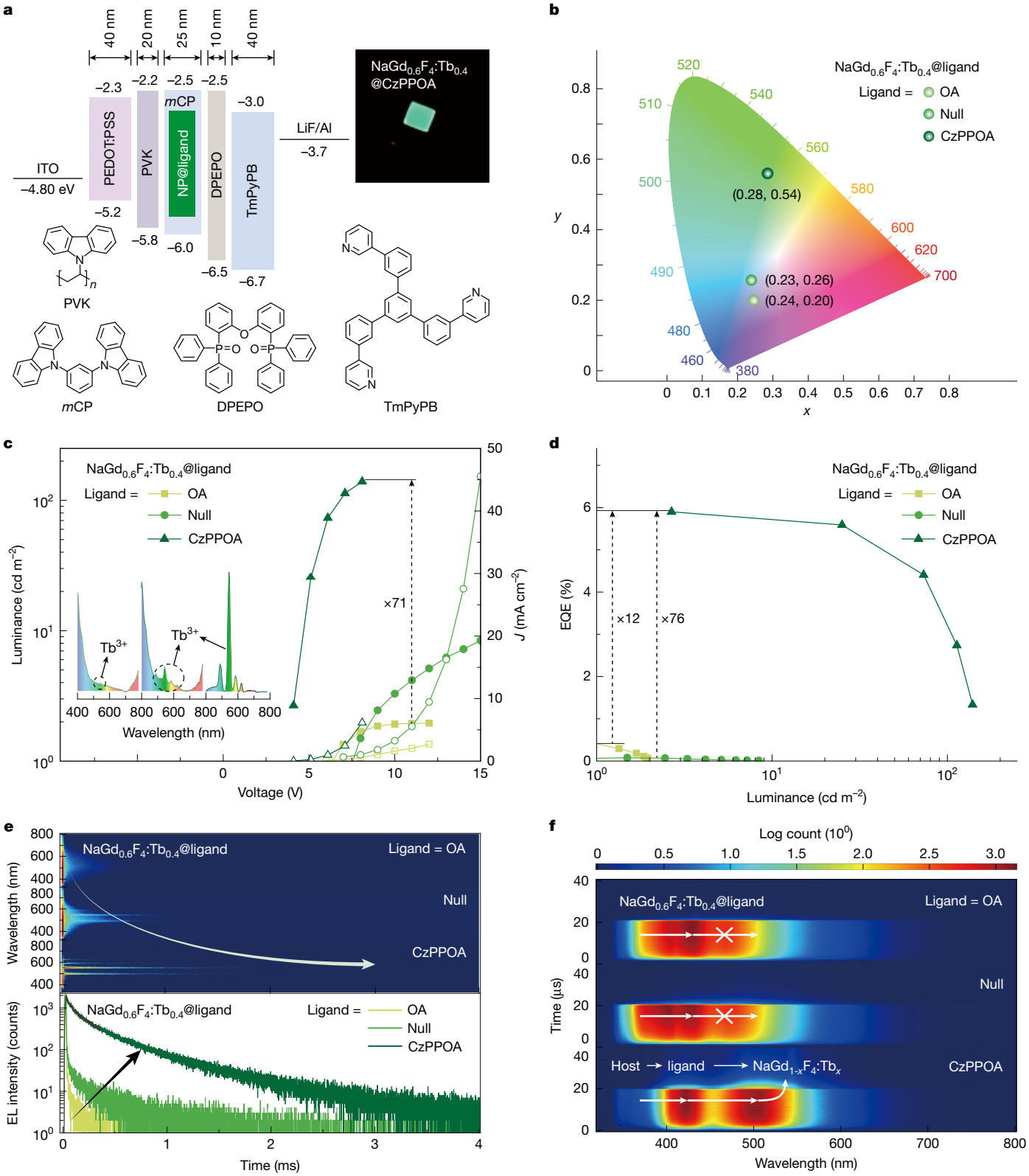

Fig. 3 | EL performance of $NaGd_{0.6}F_4:Tb_{0.4}$@ligand devices. a, Device configuration and energy-level diagram for LED devices incorporating $NaGd_{0.6}F_4:Tb_{0.4}$@ligand as the emissive layer. The chemical structures of the materials used and a photograph of a $NaGd_{0.6}F_4:Tb_{0.4}$@CzPPOA-doped device under operation at 7 V are shown. **b**, Commission Internationale de L'Eclairage coordinates of the devices plotted on the CIE1931 chromaticity plane. **c**, EL spectra (inset) and current density–voltage–luminance (*J*–*V*–*L*) characteristics of the devices. Open symbols represent current density and solid symbols denote luminance. **d**, External quantum efficiency (EQE) versus luminance curves. **e**, TREES and decay curves, showing the temporal dynamics of EL processes. **f**, Sliced TREES contours captured during carrier recombination (0–20 μs) and emission decay (20–40 μs) stages, providing insights into exciton allocation and energy-transfer mechanisms within the devices.

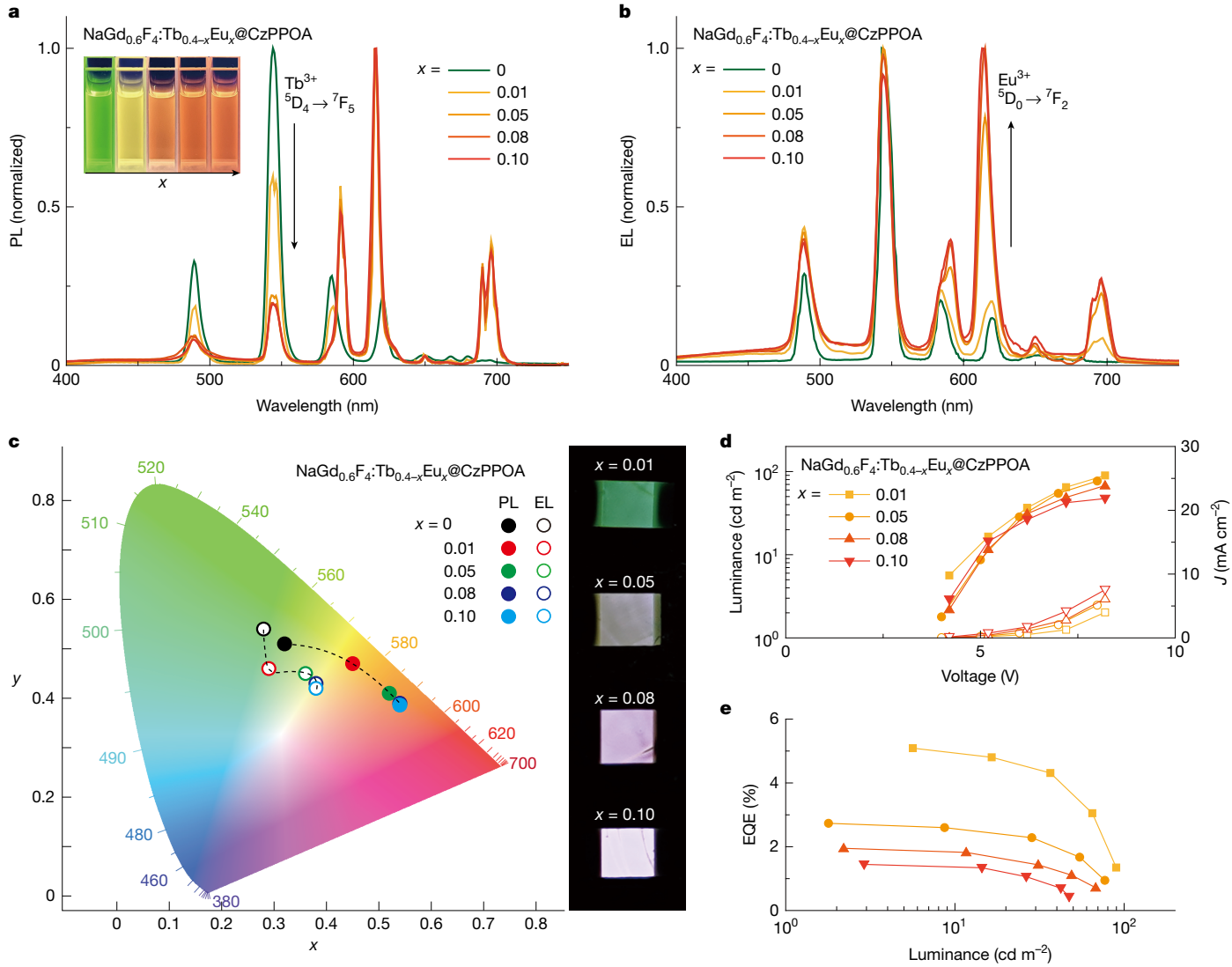

Fig. 4 | Emission characteristics of dually doped $NaGd_{0.6}F_4$:$Tb_{0.4-x}Eu_x$@CzPPOA nanocrystals. a, PL spectra of $NaGd_{0.6}F4$:$Tb_{0.4-x}Eu_x$@CzPPOA nanocrystals ($x = 0$, 0.01, 0.05, 0.08 and 1.0) dispersed in ethanol, with corresponding emission photographs shown in the inset. **b**, EL spectra of the $NaGd_{0.6}F_4$:$Tb_{0.4-x}Eu_x$@CzPPOA ($x = 0$, 0.01, 0.05, 0.08 and 0.10) based device. **c**, Variations of CIE1931 chromaticity coordinates for both thin films and devices, highlighting the colour progression from green to yellow and red with increasing Eu^{3+} content. Inset, corresponding emission photographs of the devices. **d**,**e**, Current density (J, open symbols)–voltage–luminance (solid symbols) curves (**d**) and EQE versus luminance curves (**e**) of $NaGd_{0.6}F_4$:$Tb_{0.4-x}Eu_x$@CzPPOA-based devices.

In summary, this study reports the first demonstration of efficient EL from lanthanide fluoride nanocrystals through a ligand engineering approach. By making use of the photoelectronic synergy of organic semiconductor ligands, we establish a versatile strategy that extends beyond traditional surface passivation. The engineering ligands facilitate charge and exciton confinement within the nanohybrid system, enabling effective exciton allocation to lanthanide emitters. These attributes yield EL with exceptional colour purity, spectral tunability and energy efficiency. Notably, broad spectral tunability from the visible to beyond 1,000 nm was achieved through precise control of nanocrystal doping composition and concentration, all within a fixed device architecture. These results showcase the potential of this ligand-functionalized nanocrystal platform for multiband EL emission, particularly in high-resolution and wide-gamut display technologies. However, we acknowledge several limitations of the present approach. The brightness remains constrained by the long radiative lifetimes intrinsic to lanthanide f–f transitions, as well as by the use of a simple, solution-processed trilayer device structure. Also, charge injection and transport are hindered by the insulating nature of the nanocrystal core, which constrains carrier mobility and recombination efficiency within the emissive layer. Nonetheless, this work lays a foundational framework for incorporating insulative yet optically efficient nanomaterials into functional optoelectronic devices. The demonstrated ligand-enabled strategy not only simplifies device architectures but also sets the stage for innovations in nanoscale light-emitting systems. Continued progress in ligand chemistry, charge transport engineering and device architecture optimization will be essential to fully realize the practical potential of this emerging class of emitters.

Online content

Any methods, additional references, Nature Portfolio reporting summaries, source data, extended data, supplementary information, acknowledgements, peer review information; details of author contributions and competing interests; and statements of data and code availability are available at https://doi.org/10.1038/s41586-025-09717-1.

1. Bünzli, J.-C. G. Benefiting from the unique properties of lanthanide ions. *Acc. Chem. Res.* **39**, 53–61 (2006).
2. Bünzli, J.-C. G. On the design of highly luminescent lanthanide complexes. *Coord. Chem. Rev.* **293**, 19–47 (2015).
3. Neto, A. N. C., Moura, R. T. Jr & Malta, O. L. On the mechanisms of non-radiative energy transfer between lanthanide ions: centrosymmetric systems. *J. Lumin.* **210**, 342–347 (2019).
4. Dong, H., Sun, L.-D. & Yan, C.-H. Local structure engineering in lanthanide-doped nanocrystals for tunable upconversion emissions. *J. Am. Chem. Soc.* **143**, 20546–20561 (2021).
5. Lin, Y.-C., Karlsson, M. & Bettinelli, M. in *Photoluminescent Materials and Electroluminescent Devices* (eds Armaroli, N. & Bolink, H. J.) 309–355 (Springer, 2017).
6. Huang, Y., Hsiang, E.-L., Deng, M.-Y. & Wu, S.-T. Mini-LED, micro-LED and OLED displays: present status and future perspectives. *Light Sci. Appl.* **9**, 105 (2020).
7. Moon, H., Lee, C., Lee, W., Kim, J. & Chae, H. Stability of quantum dots, quantum dot films, and quantum dot light-emitting diodes for display applications. *Adv. Mater.* **31**, 1804294 (2019).
8. Pust, P., Schmidt, P. J. & Schnick, W. A revolution in lighting. *Nat. Mater.* **14**, 454–458 (2015).
9. Jiang, W., Lee, S., Zan, G., Zhao, K. & Park, C. Alternating current electroluminescence for human-interactive sensing displays. *Adv. Mater.* **36**, 2304053 (2024).
10. Triana, M. A., Hsiang, E.-L., Zhang, C., Dong, Y. & Wu, S.-T. Luminescent nanomaterials for energy-efficient display and healthcare. *ACS Energy Lett.* **7**, 1001–1020 (2022).
11. Toninelli, C. et al. Single organic molecules for photonic quantum technologies. *Nat. Mater.* **20**, 1615–1628 (2021).
12. Guo, X., Xiang, J., Zhang, Y. & Su, Y. Integrated neuromorphic photonics: synapses, neurons, and neural networks. *Adv. Photonics Res.* **2**, 2000212 (2021).
13. Yen, M.-C. et al. All-inorganic perovskite quantum dot light-emitting memories. *Nat. Commun.* **12**, 4460 (2021).
14. Zeng, K., Shi, X., Tang, C., Liu, T. & Peng, H. Design, fabrication and assembly considerations for electronic systems made of fibre devices. *Nat. Rev. Mater.* **8**, 552–561 (2023).
15. Shirasaki, Y., Supran, G. J., Bawendi, M. G. & Bulović, V. Emergence of colloidal quantum-dot light-emitting technologies. *Nat. Photon.* **7**, 13–23 (2013).
16. Won, Y.-H. et al. Highly efficient and stable InP/ZnSe/ZnS quantum dot light-emitting diodes. *Nature* **575**, 634–638 (2019).
17. Cao, Y. et al. Perovskite light-emitting diodes based on spontaneously formed submicrometre-scale structures. *Nature* **562**, 249–253 (2018).
18. Schubert, E. F. *Light-Emitting Diodes* 2nd edn (Cambridge Univ. Press, 2006).
19. Yang, Z. et al. Recent advances in organic thermally activated delayed fluorescence materials. *Chem. Soc. Rev.* **46**, 915–1016 (2017).
20. Bünzli, J.-C. G. & Piguet, C. Taking advantage of luminescent lanthanide ions. *Chem. Soc. Rev.* **34**, 1048–1077 (2005).
21. Liu, Q. et al. Single upconversion nanoparticle imaging at sub-10 W cm^{-2} irradiance. *Nat. Photon.* **12**, 548–553 (2018).
22. Jaque, D. & Vetrone, F. Luminescence nanothermometry. *Nanoscale* **4**, 4301–4326 (2012).
23. Liu, Y., Tu, D., Zhu, H. & Chen, X. Lanthanide-doped luminescent nanoprobes: controlled synthesis, optical spectroscopy, and bioapplications. *Chem. Soc. Rev.* **42**, 6924–6958 (2013).
24. Wang, G. et al. Bifunctional strategy toward constructing perovskite/upconversion lab-on-paper photoelectrochemical device for sensitive detection of malathion. *ACS Nano* **17**, 13418–13429 (2023).
25. Leng, Y. B. et al. A near-infrared retinomorphic device with high dimensionality reservoir expression. *Adv. Mater.* **36**, 2411225 (2024).
26. Zhou, J., Zheng, G., Liu, X., Dong, G. & Qiu, J. Defect engineering in lanthanide doped luminescent materials. *Coord. Chem. Rev.* **448**, 214178 (2021).
27. Liang, Y. et al. Migrating photon avalanche in different emitters at the nanoscale enables 46th-order optical nonlinearity. *Nat. Nanotechnol.* **17**, 524–530 (2022).
28. Marin, R. & Jaque, D. Doping lanthanide ions in colloidal semiconductor nanocrystals for brighter photoluminescence. *Chem. Rev.* **121**, 1425–1462 (2020).
29. Xu, H. et al. Anomalous upconversion amplification induced by surface reconstruction in lanthanide sublattices. *Nat. Photon.* **15**, 732–737 (2021).
30. Han, S. et al. Lanthanide-doped inorganic nanoparticles turn molecular triplet excitons bright. *Nature* **587**, 594–599 (2020).
31. Carlos, L. D., Ferreira, R. A., Bermudez, V.d.Z. & Ribeiro, S. J. Lanthanide-containing light-emitting organic–inorganic hybrids: a bet on the future. *Adv. Mater.* **21**, 509–534 (2009).

Methods

Materials and instruments

All reagents and solvents used for the synthesis of the compounds were purchased from Aldrich and Acros companies and used without further purification. ^{1}H nuclear magnetic resonance (NMR) spectra were recorded using a Varian Mercury plus 400NB spectrometer, with tetramethylsilane (TMS) as the internal standard. Molecular masses were determined using a FINNIGAN LCQ electrospray ionization mass spectrometer or a matrix-assisted laser desorption/ionization time-of-flight mass spectrometer. Elemental analyses were performed using a Vario EL III elemental analyser. Suitable single crystals for X-ray diffraction analysis were obtained by slowly diffusing 12 ml of *n*-hexane into a 3-ml dichloromethane solution of ArPPOA (10 mg) at room temperature. X-ray diffraction data were collected at 295 K on a Rigaku Xcalibur E diffractometer with graphite-monochromatized Mo Kα radiation (λ = 0.71073 Å) in ω scan mode. The structures were solved using direct methods and difference Fourier syntheses. Non-hydrogen atoms were refined by full-matrix least-squares techniques on F2 with anisotropic thermal parameters. Hydrogen atoms attached to carbons were placed at calculated positions (C–H = 0.93 Å) with U(H) = 1.2Ueq(C), following the riding model approximation. All calculations were carried out using the SHELXL97 program.

We performed transmission electron microscopy measurements using a field-emission transmission electron microscope (JEOL JEM-2010F) operated at an acceleration voltage of 200 kV. Absorption and PL emission spectra were measured using a Shimadzu UV-3150 spectrophotometer and a Shimadzu RF-5301PC spectrophotometer, respectively. Cyclic voltammetry was conducted using an Eco Chemie B.V. Autolab potentiostat in a three-electrode cell with a glassy carbon working electrode, a platinum wire counter electrode and a silver/silver chloride (Ag/AgCl) reference electrode. Electrochemical experiments were carried out under a nitrogen atmosphere at room temperature in dichloromethane. Phosphorescence spectra were measured using an Edinburgh FLS1000 fluorescence spectrophotometer at 50 K.

Time decay spectra were measured using the time-correlated single photon counting method with a picosecond hydrogen lamp for the 100 ps to 10 μs range and a microsecond pulsed xenon light source for 1 μs to 10 s lifetime measurements. The synchronization photomultiplier collected the signal and the multi-channel scaling mode of the PCS900 fast counter PC plug-in card was used for data processing. Prompt and delayed fluorescence lifetimes were respectively measured with nanosecond and microsecond time decay methods. Lifetime values were simulated using an exponential fitting function in Fluoracle software.

Nanocrystal-based films (20–40 nm) for optical analysis were prepared through spin coating. The PLQYs of these films were measured using a Labsphere 1-M-2 integrating sphere (ϕ = 6″) coated by BenFlect, providing efficient light reflection across a wide range of 200–1,600 nm. The integrating sphere was coupled with the FLS1000 system. The absolute PLQY was determined by recording two spectral (emission) scans. The first spectrum captured both the scattered light and the emission from the sample, whereas the second spectrum measured the scattered light from the BenFlect coating. By integrating and subtracting the scattered light parts from both spectra, we determined the photon number absorbed by the sample (N_a). The emission of the sample was integrated to calculate the emissive photon number (N_e). The absolute PLQY (η) was then calculated using the equation $\eta = N_e/N_a$. Spectral correction (emission arm) was applied to the raw data after background subtraction and the quantum yield was calculated from the spectrally corrected curves using the F900 software wizard.

Synthesis details

$NaGd_{1-x}F_4$:Tb/Eu_x@OA nanocrystals: Lanthanide nanocrystals were synthesized according to a well-documented coprecipitation method[30]. In a typical experiment for synthesizing $NaGd_{1-x}F_4$:Tb_x nanocrystals, $GdCl_3 \cdot 6H_2O$ (1-*x* mmol) and $TbCl_3 \cdot 6H_2O$ or $EuCl_3 \cdot 6H_2O$ (*x* mmol) were mixed with OA (6 ml) and 1-octadecene (15 ml) in a 100-ml flask. The mixture was heated to 140 °C for 3 h. After cooling to 50 °C, a methanol solution (10 ml) containing NaOH (0.1 g, 2.5 mmol) and NH_4F (0.148 g, 4 mmol) was added and the mixed solution was stirred for 12 h. The temperature was then raised to 70 °C to remove methanol. After that, the solution was heated to 240 °C under an argon atmosphere for 45 min, followed by cooling to room temperature. The resulting nanocrystals were extracted by repeated precipitation with a mixture of ethanol and hexane, collected by centrifugation at 12,000 rpm for 5 min and redispersed in 9 ml of hexane.

$NaGd_{0.6}F_4$:$Tb_{0.4-x}$Eu@OA nanocrystals. The synthesis followed the same procedure as above, with the inclusion of $EuCl_3 \cdot 6H_2O$ (*x* mmol, *x* = 0.01, 0.05, 0.08 or 0.10).

Preparation of ligand-free nanocrystals. In a typical process[32], 1 ml of the as-prepared OA-capped nanocrystals dispersion in hexane (about 50 mg ml^{-1}) was combined with 1 ml of a *N*,*N*-dimethylformamide (DMF) solution containing $NOBF_4$ (0.011 g, 0.1 mmol) at room temperature. The mixture was ultrasonicated for 20 min to remove oleate ligands on the surface, followed by the addition of 1 ml of toluene and further sonication for another 20 min. The ligand-free nanocrystals were collected by centrifugation and redispersed in DMF (1 ml). For purification, 1 ml of a hexane–toluene solution (1:1 v/v) was added to flocculate the dispersion and the precipitate was collected by means of centrifugation. The nanocrystals were then redispersed in 2 ml of EtOH to form a stable colloidal dispersion.

Surface ligand modification. For ligand modification, sodium hydroxide (0.002 g, 0.05 mmol) in 1 ml of ethanol was added to the desired ligand (0.05 mmol) in 2 ml of ethanol to prepare a ligand salt solution. This solution was added to an ethanol dispersion of ligand-free nanocrystals (0.001 mmol) and ultrasonicated for two hours to ensure ligand coordination to nanocrystal surfaces. Excess ligand was removed by centrifugation and the modified nanocrystals were redispersed in ethanol for optical measurements or in DMF for device fabrication.

Diphenyl(*o*-tolyl)phosphine oxide (TPPOM). Under an argon atmosphere, 1-bromo-2-methylbenzene (1.186 ml, 10 mmol) in 10 ml of dry ether was added dropwise to a mixture of magnesium turnings (0.267 g, 11 mmol) and a small piece of iodine in 10 ml of dry ether at room temperature. The reaction was stirred at 40 °C for one hour. After cooling to 0 °C, chlorodiphenylphosphine (1.980 ml, 11 mmol) in 10 ml of dry ether was added dropwise and stirred for 12 h. The reaction was quenched by adding water and the mixture was extracted with CH_2Cl_2 (3 × 30 ml). The CH_2Cl_2 solution was concentrated to 30 ml, then 30% H_2O_2 (4.5 ml, 40 mmol) was added at 0 °C and stirred for four hours. After another extraction with CH_2Cl_2 (3 × 30 ml), the organic phase was combined and dried with anhydrous Na_2SO_4. The solvent was removed in vacuo. The product was purified by flash column chromatography, affording 2.6 g of white powder in 90% yield. ^{1}H NMR (TMS, $CDCl_3$, 400 MHz): δ = 7.708–7.612 (m, 4H), 7.591–7.519 (m, 2H), 7.515–7.390 (m, 5H), 7.319–7.270 (m, 1H), 7.115 (t, J = 7.2 Hz, 1H), 6.998 (q, J_1 = 13.6 Hz, J_2 = 7.2 Hz, 1H), 2.453 ppm (s, 3H). Laser desorption/ionization time-of-flight (LDI-TOF): *m*/*z* (%): 292.10 (100) [M^+]; elemental analysis (%) for $C_{19}H_{17}OP$: C 78.07, H 5.86, O 5.47; found: C 78.09, H 5.89, O 5.50.

(4-bromo-2-methylphenyl)diphenylphosphine oxide (TPPOMBr). The synthetic procedure was similar to that of TPPOM except for using 4-bromo-1-iodo-2-methylbenzene (2.959 g, 10 mmol) instead of 1-bromo-2-methylbenzene. The product yielded 3.3 g of white powder (90% yield). ^{1}H NMR (TMS, DMSO-d_6, 400 MHz): δ = 7.680–7.605 (m, 3H), 7.604–7.525 (m, 8H), 7.489 (d, J = 8.0 Hz, 1H), 6.857 (q, J_1 = 13.2 Hz,

J_2 = 8.4 Hz, 1H), 2.288 ppm (s, 3H). LDI-TOF: *m/z* (%): 370.01 (100) [M^+]; elemental analysis (%) for $C_{19}H_{16}BrOP$: C 61.48, H 4.34, O 4.31; found: C 61.50, H 4.36, O 4.35.

(4-(9H-carbazol-9-yl)-2-methylphenyl)diphenylphosphine oxide (CzPPOM). Under an argon atmosphere, TPPOMBr (1.856 g, 5 mmol), carbazole (2.508 g, 15 mmol), CuI (0.095 g, 0.5 mmol) and K_2CO_3 (2.073 g, 15 mmol) were dissolved in 50 ml of 1,3-dimethyl-2-imidazolidinone (DMI) and heated to 190 °C for 12 h. After cooling to room temperature, the mixture was poured into water and extracted with dichloromethane (3 × 10 ml) again. The organic layers were combined and dried with anhydrous Na_2SO_4 and the solvent was removed in vacuo. The crude product was purified by column chromatography, affording 1.8 g of white powder (80% yield). ^{1}H NMR (TMS, DMSO-d_6, 400 MHz): δ = 8.231 (d, J = 7.6 Hz, 2H), 7.753–7.694 (m, 3H), 7.693–7.643 (m, 4H), 7.644–7.577 (m, 4H), 7.542 (d, J = 8.0 Hz, 1H), 7.497 (d, J = 8.0 Hz, 2H), 7.411 (t, J = 7.6 Hz, 2H), 7.279 (t, J = 7.2 Hz, 2H), 7.209 (q, J_1 = 13.6 Hz, J_2 = 8.4 Hz, 1H), 2.432 ppm (s, 3H). LDI-TOF: *m/z* (%): 457.16 (100) [M^+]; elemental analysis (%) for $C_{31}H_{24}NOP$: C 81.38, H 5.29, N 3.06, O 3.50; found: C 81.39, H 5.30, N 3.08, O 3.54.

(4-(3,6-di-*tert*-butyl-9H-carbazol-9-yl)-2-methylphenyl)diphenylphosphine oxide (tBCzPPOM). The synthetic procedure was similar to that of CzPPOM except for using 3,6-di-*tert*-butyl-carbazole (4.188 g, 15 mmol) instead of carbazole. The yield was 2.2 g of white powder (80% yield). ^{1}H NMR (TMS, $CDCl_3$, 400 MHz): δ = 8.138 (s, 2H), 7.711 (q, J_1 = 11.6 Hz, J_2 = 7.6 Hz, 4H), 7.480 (s, 1H), 7.448–7.332 (m, 10H), 7.299 (d, J = 8.0 Hz, 1H), 7.220 (q, J_1 = 13.2 Hz, J_2 = 8.0 Hz, 1H), 2.515 (s, 3H), 1.385 ppm (s, 18H). LDI-TOF: *m/z* (%): 569.28 (100) [M^+]; elemental analysis (%) for $C_{39}H_{40}NOP$: C 82.22, H 7.08, N 2.46, O 2.81; found: C 82.25, H 7.07, N 2.50, O 2.83.

(4-(9,9-dimethylacridin-10(9H)-yl)-2-methylphenyl)diphenylphosphine oxide (DMACPPOM). In an argon atmosphere, *tris*(dibenzylideneacetone)dipalladium (0.366 g, 0.4 mmol) and (t-Bu)$_3$P (0.094 ml, 0.4 mmol) were mixed in toluene (10 ml) and stirred for 20 min at room temperature. TPPOMBr (3.700 g, 10 mmol), 9,9-dimethyl-9,10-dihydroacridine (DMAC, 2.509 g, 12 mmol), t-BuONa (1.922 g, 20 mmol) were added and the mixture was heated to 90 °C and stirred for six hours. After the reaction, the toluene solvent was removed by distillation and the solid was dissolved in dichloromethane. The crude product was purified by flash column chromatography, yielding 3.9 g of pale-yellow powder (80% yield). ^{1}H NMR (TMS, $CDCl_3$, 400 MHz): δ = 7.739 (q, J_1 = 12.0 Hz, J_2 = 6.8 Hz, 4H), 7.581 (t, J = 7.2 Hz, 2H), 7.570–7.499 (m, 4H), 7.438 (dd, J_1 = 7.6 Hz, J_2 = 1.2 Hz, 2H), 7.305–7.267 (m, 1H), 7.268–7.215 (m, 1H), 7.120 (d, J = 8.0 Hz, 1H), 6.978 (t, J = 7.2 Hz, 2H), 6.920 (t, J = 7.2 Hz, 2H), 6.266 (d, J = 8.0 Hz, 2H), 2.519 (s, 3H), 1.667 ppm (s, 6H). LDI-TOF: *m/z* (%): 499.21 (100) [M^+]; elemental analysis (%) for $C_{34}H_{30}NOP$: C 81.74, H 6.05, N 2.80, O 3.20; found: C 81.75, H 6.06, N 2.84, O 3.22.

(4-(9,9-diphenylacridin-10(9H)-yl)-2-methylphenyl)diphenylphosphine oxide (DPACPPOM). The synthetic procedure was similar to that of DMACPPOM except for using 9,9-diphenyl-9,10-dihydroacridine (DPAC, 3.998 g, 12 mmol) instead of DMAC. The reaction yielded 4.9 g of white powder with an 80% yield. ^{1}H NMR (TMS, $CDCl_3$, 400 MHz): δ = 7.689 (q, J_1 = 12.0 Hz, J_2 = 7.2 Hz, 4H), 7.567 (t, J = 7.2 Hz, 2H), 7.550–7.464 (m, 4H), 7.291–7.193 (m, 6H), 7.126 (q, J_1 = 13.6 Hz, J_2 = 8.0 Hz, 1H), 7.112–7.039 (m, 2H), 7.004–6.927 (m, 5H), 6.922–6.843 (m, 5H), 6.425 (d, J = 8.0 Hz, 2H), 2.444 ppm (s, 3H). LDI-TOF: *m/z* (%): 623.24 (100) [M^+]; elemental analysis (%) for $C_{44}H_{34}NOP$: C 84.73, H 5.49, N 2.25, O 2.57; found: C 84.74, H 5.51, N 2.28, O 2.60.

2-(diphenylphosphoryl)benzoic acid (TPPOA). Powdered $KMnO_4$ (3.161 g, 20 mmol) was added in four portions over 1.5 h to a boiling mixture of diphenyl(*o*-tolyl)phosphine oxide (TPPOM) (1.461 g, 5 mmol), pyridine (25 ml) and water (10 ml), maintaining gentle boiling throughout. The mixture was boiled for 5 h, after which pyridine and water were removed by distillation. On cooling to room temperature, 1 ml (6 mmol ml^{-1}) of hydrochloric acid in 10 ml of H_2O was added dropwise and stirred for 30 min. The mixture was extracted with water and chloroform (3 × 10 ml). The organic layers were combined and dried with anhydrous Na_2SO_4. The solvent was removed in vacuo. The crude product was purified by column chromatography, yielding 1.1 g of white powder with a yield of 70%. ^{1}H NMR (TMS, DMSO-d_6, 400 MHz): δ = 13.086 (s, 1H), 7.904–7.845 (m, 1H), 7.701 (t, J = 7.6 Hz, 1H), 7.628 (t, J = 7.6 Hz, 1H), 7.610–7.539 (m, 5H), 7.539–7.455 ppm (m, 6H). LDI-TOF: *m/z* (%): 322.08 (100) [M^+]; elemental analysis (%) for $C_{19}H_{15}O_3P$: C 70.81, H 4.69, O 14.89; found: C 70.83, H 4.69, O 14.91.

5-(9H-carbazol-9-yl)-2-(diphenylphosphoryl)benzoic acid (CzPPOA). The synthetic procedure was analogous to that of TPPOA but with the substitution of CzPPOM (2.286 g, 5 mmol) for TPPOM. The reaction produced 0.9 g of white powder with a 40% yield. ^{1}H NMR (TMS, DMSO-d_6, 400 MHz): δ = 13.386 (s, 1H), 8.256 (d, J = 7.6 Hz, 2H), 8.090 (t, J = 2.0 Hz, 1H), 7.975 (d, J = 8.4 Hz, 1H), 7.762 (q, J_1 = 12.8 Hz, J_2 = 8.4 Hz, 1H), 7.738–7.645 (m, 4H), 7.642–7.588 (m, 2H), 7.588-7.510 (m, 6H), 7.447 (t, J = 7.6 Hz, 2H), 7.314 ppm (t, J = 7.6 Hz, 2H). LDI-TOF: *m/z* (%): 487.13 (100) [M^+]; elemental analysis (%) for $C_{31}H_{22}NO_3P$: C 76.38, H 4.55, N 2.87, O 9.85; found: C 76.39, H 4.57, N 2.89, O 9.88.

5-(3,6-di-*tert*-butyl-9H-carbazol-9-yl)-2-(diphenylphosphoryl) benzoic acid (tBCzPPOA). The synthetic procedure was similar to that of TPPOA except for using tBCzPPOM (2.846 g, 5 mmol) instead of TPPOM. The reaction yielded 1.2 g of white powder with a 40% yield. ^{1}H NMR (TMS, DMSO-d_6, 400 MHz): δ = 13.359 (s, 1H), 8.324 (s, 2H), 8.077 (s, 1H), 7.977 (d, J = 6.8 Hz, 1H), 7.821–7.720 (m, 1H), 7.718–7.631 (m, 4H), 7.629–7.527 (m, 6H), 7.525–7.424 (m, 4H), 1.416 ppm (s, 18H). LDI-TOF: *m/z* (%): 599.26 (100) [M^+]; elemental analysis (%) for $C_{39}H_{38}NO_3P$: C 78.11, H 6.39, N 2.34, O 8.00; found: C 78.13, H 6.37, N 2.37, O 8.03.

5-(9,9-dimethylacridin-10(9H)-yl)-2-(diphenylphosphoryl)benzoic acid (DMACPPOA). The synthetic procedure was similar to that of TPPOA except that DMACPPOM (2.496 g, 5 mmol) was used instead of TPPOM. The reaction gave 1.0 g of pale-yellow powder with a 40% yield. ^{1}H NMR (TMS, $CDCl_3$, 400 MHz): δ = 8.392 (s, 1H), 7.750–7.548 (m, 9H), 7.545–7.432 (m, 5H), 7.324–7.254 (m, 2H), 7.252–7.175 (m, 2H), 7.128 (t, J = 7.2 Hz, 1H), 7.036 (d, J = 7.6 Hz, 1H), 1.486 ppm (s, 6H). LDI-TOF: *m/z* (%): 529.18 (100) [M^+]; elemental analysis (%) for $C_{34}H_{28}NO_3P$: C 77.11, H 5.33, N 2.64, O 9.06; found: C 77.11, H 5.32, N 2.67, O 9.08.

5-(9,9-diphenylacridin-10(9H)-yl)-2-(diphenylphosphoryl)benzoic acid (DPACPPOA). The synthetic procedure was similar to that of TPPOA except that DMACPPOM (3.116 g, 5 mmol) was used instead of TPPOM. The reaction yielded 1.3 g of white powder with a 40% yield. ^{1}H NMR (TMS, $CDCl_3$, 400 MHz): δ = 8.097 (s, 1H), 7.652–7.527 (m, 6H), 7.524–7.423 (m, 4H), 7.294–7.165 (m, 6H), 7.106 (t, J = 7.2 Hz, 2H), 7.028 (q, J_1 = 14.0 Hz, J_2 = 8.0 Hz, 1H), 7.000–6.854 (m, 9H), 6.572 ppm (d, J = 8.0 Hz, 2H). LDI-TOF: *m/z* (%): 653.21 (100) [M^+]; elemental analysis (%) for $C_{44}H_{32}NO_3P$: C 80.84, H 4.93, N 2.14, O 7.34; found: C 80.86, H 4.92, N 2.16, O 7.38.

Nanohybrid synthesis. To prepare the ligand salt solution, sodium hydroxide (0.002 g, 0.05 mmol) in 1 ml of ethanol was added into a mixture of 0.05 mmol of ligand in 2 ml of ethanol. This ligand salt solution was then combined with an ethanol solution containing ligand-free nanocrystals (0.001 mmol) and the mixture was ultrasonicated for two hours to ensure proper ligand coordination of the ligands to nanocrystal surfaces. Any excess ligand was removed by centrifugation and the resulting product was redispersed in ethanol for optical measurements or in DMF for device fabrication.

Preparation of Tb(ligand)$_3$ complexes. Tb(ligand)$_3$ complexes were prepared according to established protocols[33]. ArPPOA (3 mmol) was dissolved in 10 ml of ethanol and NaOH (0.120 g, 3 mmol) in aqueous solution (1 M) was added to deprotonate ArPPOA. $TbCl_3{\cdot}6H_2O$ (0.373 g, 1 mmol) in 0.1 ml of water was added dropwise, then the solution was stirred at 60 °C for two hours. The product was purified by precipitation using a concentrated ethanol–water solution.

Device fabrication. The device structure consisted of: ITO|PEDOT:PSS (40 nm)|PVK (20 nm)|*m*CP:*y* wt% $NaGd_{0.6}F_4$:$Tb_{0.4-x}Eu_x$@ligand (25 nm)|DPEPO (10 nm)|TmPyPB (40 nm)|LiF (1 nm)|Al (100 nm). In this configuration, poly(3,4-ethylenedioxythiophene):poly(styrenesulfonate) (PEDOT:PSS) and LiF serve as the hole and electron injection layers, respectively, whereas the other materials, including polyvinylcarbazole (PVK), 1,3-bis(*N*-carbazolyl)benzene (*m*CP), *bis*[2-(diphenylphosphino) phenyl] ether oxide (DPEPO) and 1,3,5-tri[(3-pyridyl)-phen-3-yl]benzene (TmPyPB), function as hole transporting, host, exciton blocking and electron transporting layers, respectively. Further host materials such as bis-4-(*N*-carbazolyl)phenyl)phenylphosphine oxide (BCPO), 4,4′-bis(9H-carbazol-9-yl)biphenyl (CBP), 4,4-bis(9-carbazolyl)-2,2-dimethylbiphenyl (CDBP), CPPOM, 9-(4-*tert*-butylphenyl)-3,6-bis(triphenylsilyl)-9H-carbazole (CzSi), DPEPO and PVK were also used for comparison. The PEDOT:PSS layer was spin-coated on a patterned ITO-coated glass substrate after oxygen plasma treatment. To remove any residual water, the PEDOT:PSS layer was baked at 120 °C for 20 min in a glovebox. The PVK layer was then spin-coated from a 10 mg ml^{-1} DMF solution onto the PEDOT:PSS layer and baked at 70 °C for 15 min. The emitting layer, also spin-coated from DMF at a concentration of 10 mg ml^{-1}, was similarly baked at 70 °C for 15 min. After spin-coating, the sample was transferred to a high-vacuum evaporation system. The electron transporting layers were sequentially evaporated at a rate of 0.1-0.2 nm s^{-1} under a pressure less than 4×10^{-4} Pa. A 1-nm-thick LiF layer was deposited at 0.1 nm s^{-1} to improve electron injection, followed by a 100-nm-thick Al cathode deposited at 0.6 nm s^{-1}. The emission area of the devices was 0.09 cm^2, defined by the overlap of the anode and cathode. Post-fabrication, all devices were encapsulated with ultraviolet epoxy resin in the glovebox before undergoing luminance–current–voltage measurements. Emission intensity was measured with a calibrated Si photodiode and the external quantum efficiency was calculated assuming a Lambertian distribution. The electroluminescent spectrum was recorded using a calibrated PR-655 spectrometer.

Absorption and luminescence spectroscopy analysis. Absorption spectra in the near-infrared range were measured at room temperature using a Shimadzu ultraviolet–visible–near-infrared spectrophotometer (UV-3600). PL spectra were recorded at room temperature using a DM150i monochromator and an R928 photon-counting photomultiplier tube, in conjunction with a 980-nm diode laser. Decay curves were measured with a custom ultraviolet-to-mid-infrared phosphorescence lifetime spectrometer (FLS1000, Edinburgh) equipped with a digital oscilloscope (TDS3052B, Tektronix) and a tunable optical parametric oscillator laser (410–2,400 nm, Vibrant 355 II, OPOTEK) as the excitation source.

Transient absorption spectroscopy. Transient absorption spectra were recorded using a pump–probe set-up. Samples were excited by tunable pump pulses (355–2,600 nm) generated from an optical parametric amplifier, pumped by a regenerative Ti:sapphire amplifier (Coherent; 800 nm, 100 fs, 7 mJ per pulse, 1 kHz repetition rate). Broadband probe pulses were generated by focusing a portion of the Ti:sapphire output onto a sapphire crystal or YAG crystal, producing light spanning 350–1,550 nm. For short-time measurements (500 fs to 7 ns), a commercial spectrometer (HELIOS, Ultrafast Systems) was used, with probe ranges of 350–800 nm and 750–1,600 nm. Long-time measurements (1 ns to 1 ms) used probe ranges of 410–750 nm and 850–1,600 nm. A computer-controlled motorized delay stage was used to vary the probe path length. The pump beam was modulated at 500 Hz using a chopper, generating alternating probe pulses with and without excitation. Both beams were focused to an approximately 0.5-mm^2 spot on the sample. The instrument response function was approximately 200 fs.

Femtosecond sum-frequency upconversion spectroscopy. PL decay kinetics within a 7-ns window were recorded using a femtosecond sum-frequency upconversion apparatus (HALCYONE, Ultrafast Systems) powered by a regenerative Ti:sapphire amplifier (Coherent; 800 nm, 100 fs, 7 mJ per pulse, 1 kHz repetition rate). The 800-nm beam was split: one portion pumped an optical parametric amplifier to produce tunable excitation pulses and the other served as the gate pulse. Emission from the sample was collected and co-focused with the 800-nm gate pulse onto a barium metaborate crystal, generating an upconverted signal by means of sum-frequency generation. This signal was passed through a 300-mm monochromator and detected by a spectrometer, providing a temporal resolution of 250 ps. All measurements were conducted on samples sealed in 2-mm airtight cuvettes, placed in a nitrogen-filled glovebox under continuous agitation.

Data availability

All relevant data that support the findings of this work are available from the corresponding author on request.

32. Dong, A. et al. A generalized ligand-exchange strategy enabling sequential surface functionalization of colloidal nanocrystals. *J. Am. Chem. Soc.* **133**, 998–1006 (2011).
33. Melby, L. R., Rose, N. J., Abramson, E. & Caris, J. C. Synthesis and fluorescence of some trivalent lanthanide complexes. *J. Am. Chem. Soc.* **86**, 5117–5125 (1964).

Acknowledgements This work was supported by the RIE2025 Manufacturing, Trade and Connectivity (MTC) Programmatic Fund (award no. M21J9b0085) and the National Natural Science Foundation of China (award nos. 22325502, 92061205, 52273173, 22305073, 22371162 and 22005088), Guangdong Basic and Applied Basic Research Fund (2024A1515010713), the Guangdong Innovative and Entrepreneurial Research Team Program (2023ZT10C040) and the Overseas Research Cooperation Fund of Tsinghua SIGS (HW2023002), the Changjiang Scholars Program of the Chinese Ministry of Education (award no. Q2021256) and the Research Grants Council of Hong Kong for a Research Fellow Award (grant no. RFS2021-1S03).

Author contributions H.X. and X.L. conceived, designed and supervised the project and led the collaboration efforts. J.T., P.Z., X.S. and S.H. synthesized nanohybrids, spectroscopy study and conducted optoelectronic experiments, with contributions from F.W., J.Z. C.D. and Z.Z. J.T., P.Z., H.X., S.H., C.H. and X.L. wrote the manuscript. All authors participated in the discussion and analysis of the manuscript.

Competing interests The authors declare no competing interests.

Additional information

Supplementary information The online version contains supplementary material available at https://doi.org/10.1038/s41586-025-09717-1.

Correspondence and requests for materials should be addressed to Chunmiao Han, Sanyang Han, Hui Xu or Xiaogang Liu.

Peer review information *Nature* thanks Houman Bahmani Jalali, Fernando Sigoli and the other, anonymous, reviewer(s) for their contribution to the peer review of this work.

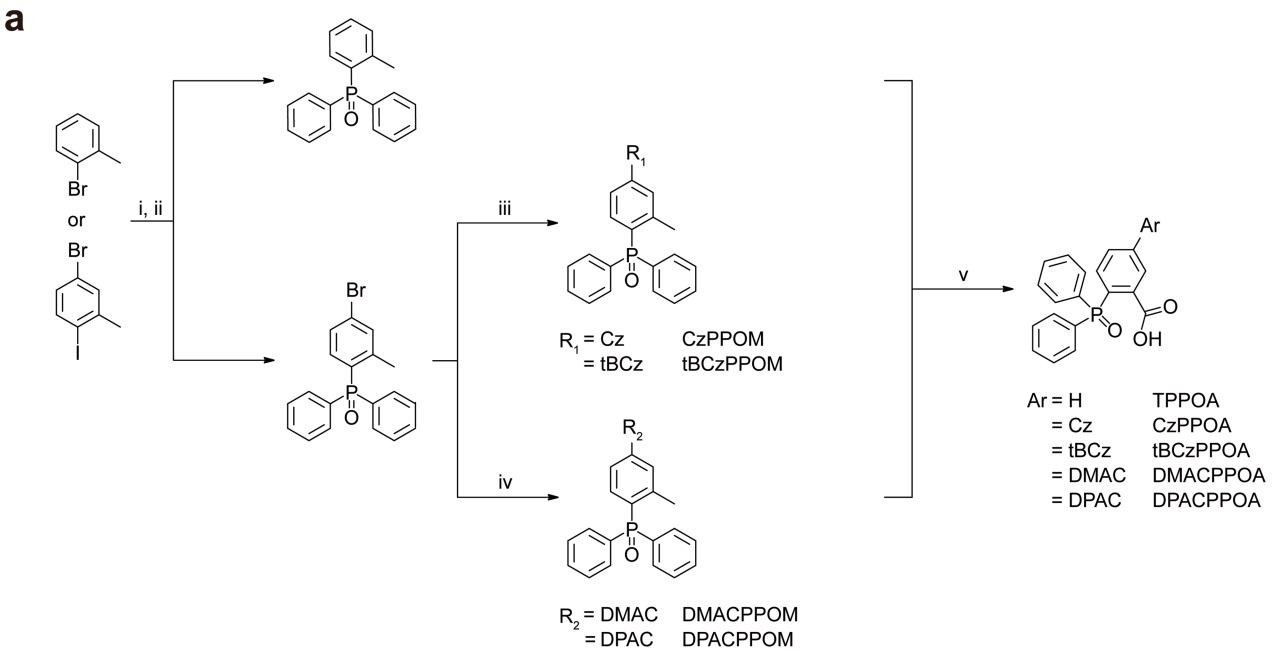

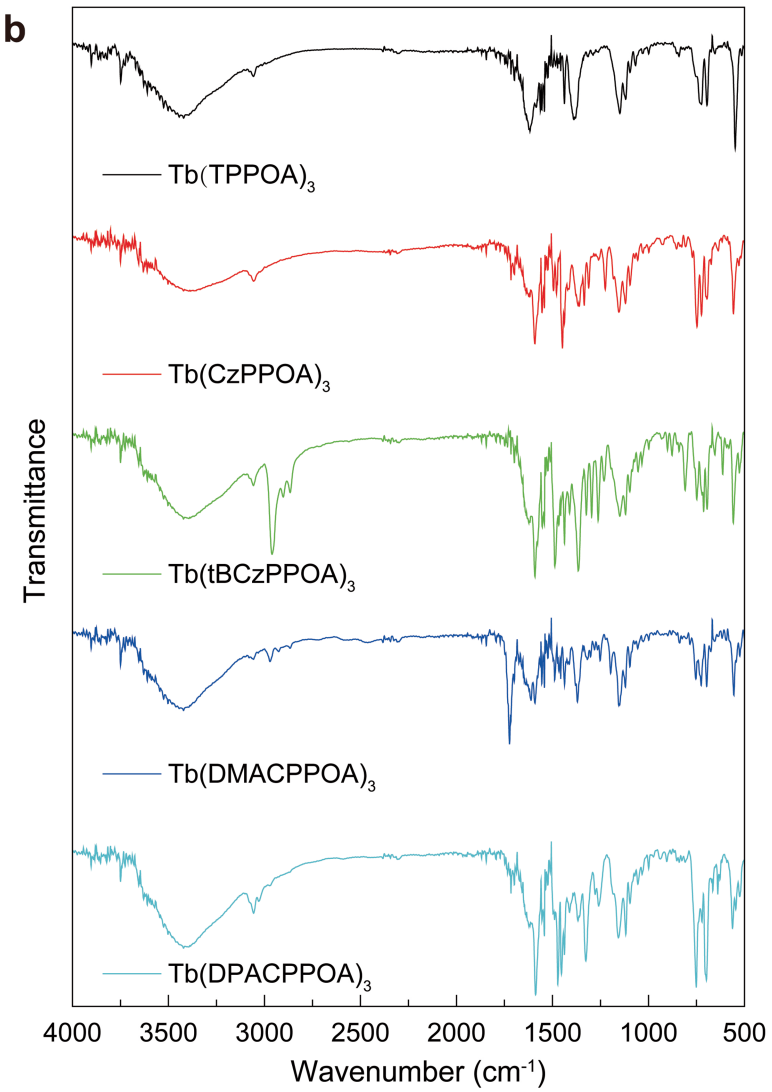

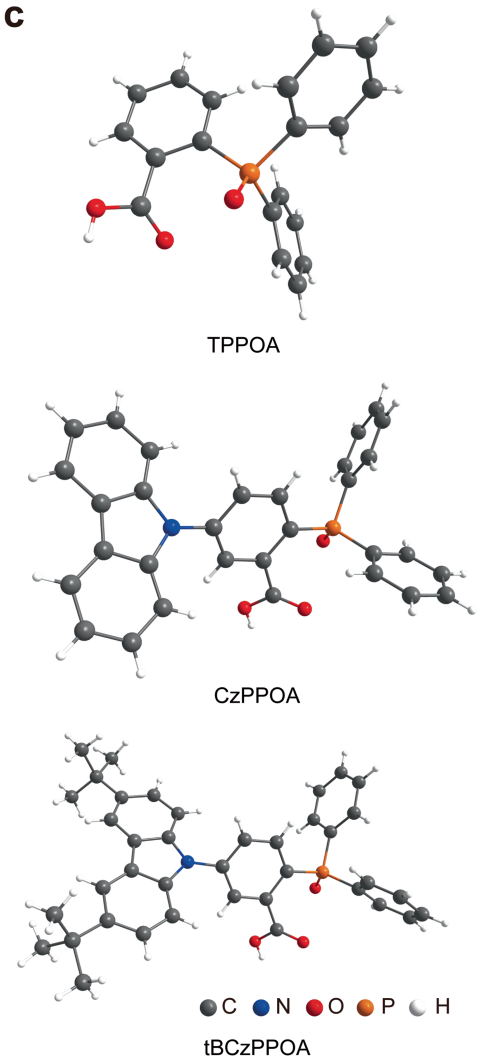

Extended Data Fig. 1 | See next page for caption.

Extended Data Fig. 1 | Synthesis and characterization of ArPPOA ligands. **a**, Synthetic procedures of TPPOA, CzPPOA, tBCzPPOA, DMACPPOA and DPACPPOA. i. Mg, Et_2O, 40 °C, 1 h; Ph_2PCl, Et_2O, 0 °C, 12 h; ii. 30% H_2O_2, CH_2Cl_2, 0 °C, 4 h; iii. carbazole/3,6-di-tert-butyl-carbazole, K_2CO_3, CuI, DMI, 190 °C, 12 h; iv. $Pd_2(dba)_3$, (*t*-Bu)$_3$P, toluene, room temperature, 20 min; 9,9-dimethyl-9,10-dihydroacridine/9,9-diphenyl-9,10-dihydroacridine, *t*-BuONa, 90 °C, 6 h; v. $KMnO_4$, pyridine, H_2O, 6 h. **b**, Fourier-transform infrared spectra of $Tb(TPPOA)_3$, $Tb(CzPPOA)_3$, $Tb(tBCzPPOA)_3$, $Tb(DMACPPOA)_3$ and $Tb(DPACPPOA)_3$ in KBr pellets. The peaks around 1,150 cm^{-1} and 1,437 cm^{-1} are assigned to the characteristic absorption peaks originating from P=O and C-P in ArPPOA. Also, the peaks around 1,472 and 1,576 cm^{-1} are attributed to the symmetric (ν_s) and asymmetric (ν_{as}) modes of the carboxyl groups (−COO−). The band around 1,716 cm^{-1} arises from the stretching vibration of the C=O group. **c**, Single-crystal structures of TPPOA, CzPPOA and tBCzPPOA.

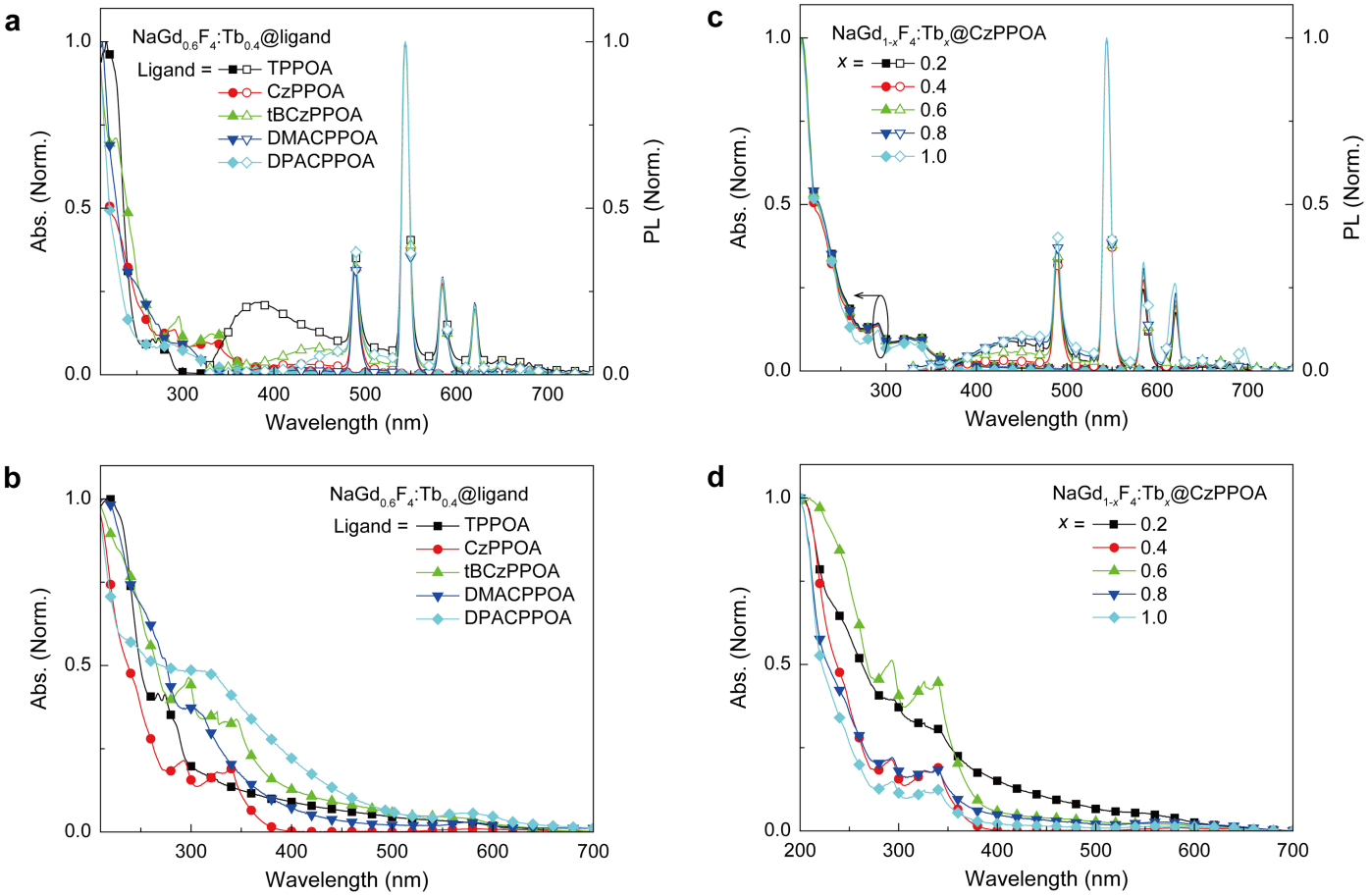

Extended Data Fig. 2 | Absorption and PL spectra of hybrid nanocrystals modified with different types of ArPPOA molecule and doped with Tb^{3+} ions at varying concentrations. Comparison of the absorption and steady-state PL spectra of $NaGd_{0.6}F_4$:$Tb_{0.4}$@ligand in EtOH (2 mg ml^{-1}) (**a**) and films (**b**). Doping concentration dependence of absorption and steady-state PL spectra for $NaGd_{1-x}F_4$:Tb_x@CzPPOA in EtOH (2 mg ml^{-1}) (**c**) and films (**d**) (x = 0.2–1.0).

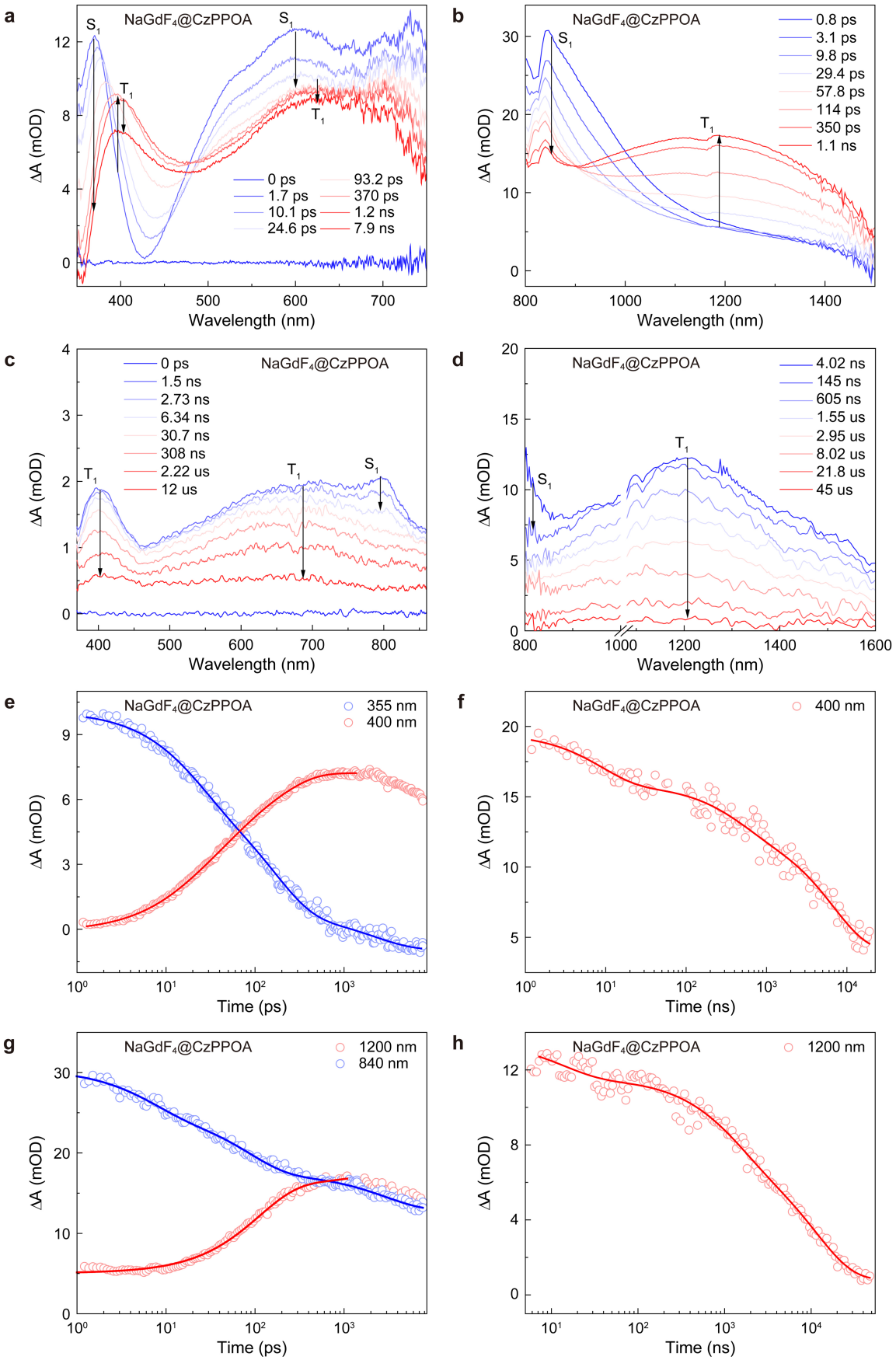

Extended Data Fig. 3 | See next page for caption.

Extended Data Fig. 3 | Transient absorption spectra and kinetics of $NaGdF_4$@CzPPOA. The femtosecond transient absorption spectra of the $NaGdF_4$@CzPPOA nanohybrids are presented for the visible region (**a**) and the near-infrared region (**b**) and nanosecond transient absorption spectra are shown for the visible region (**c**) and the near-infrared region (**d**). The corresponding dynamics were extracted from the femtosecond spectrum for the visible region (**e**) and the near-infrared region (**f**) and from the nanosecond spectrum for the visible region (**g**) and the near-infrared region (**h**).

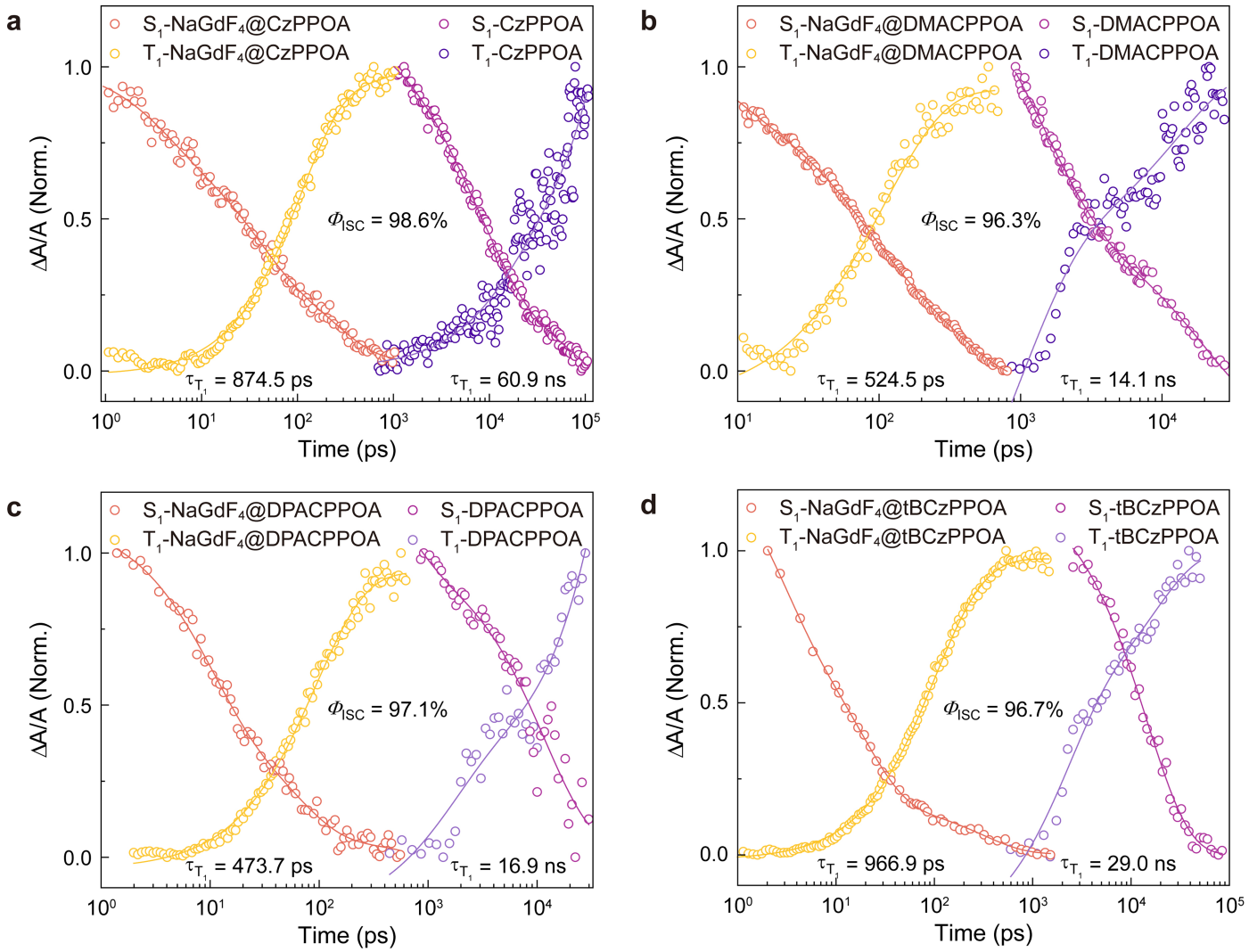

Extended Data Fig. 4 | Singlet and triplet dynamics of different ArPPOA molecules on the surface of $NaGdF_4$ nanocrystals. Extracted kinetics showing the singlet decay and triplet growth of a solution containing pristine molecules and of a solution of ligand-molecule-modified $NaGdF_4$ nanocrystals: CzPPOA (**a**), DMACPPOA (**b**), DPACPPOA (**c**), and tBCzPPOA (**d**).

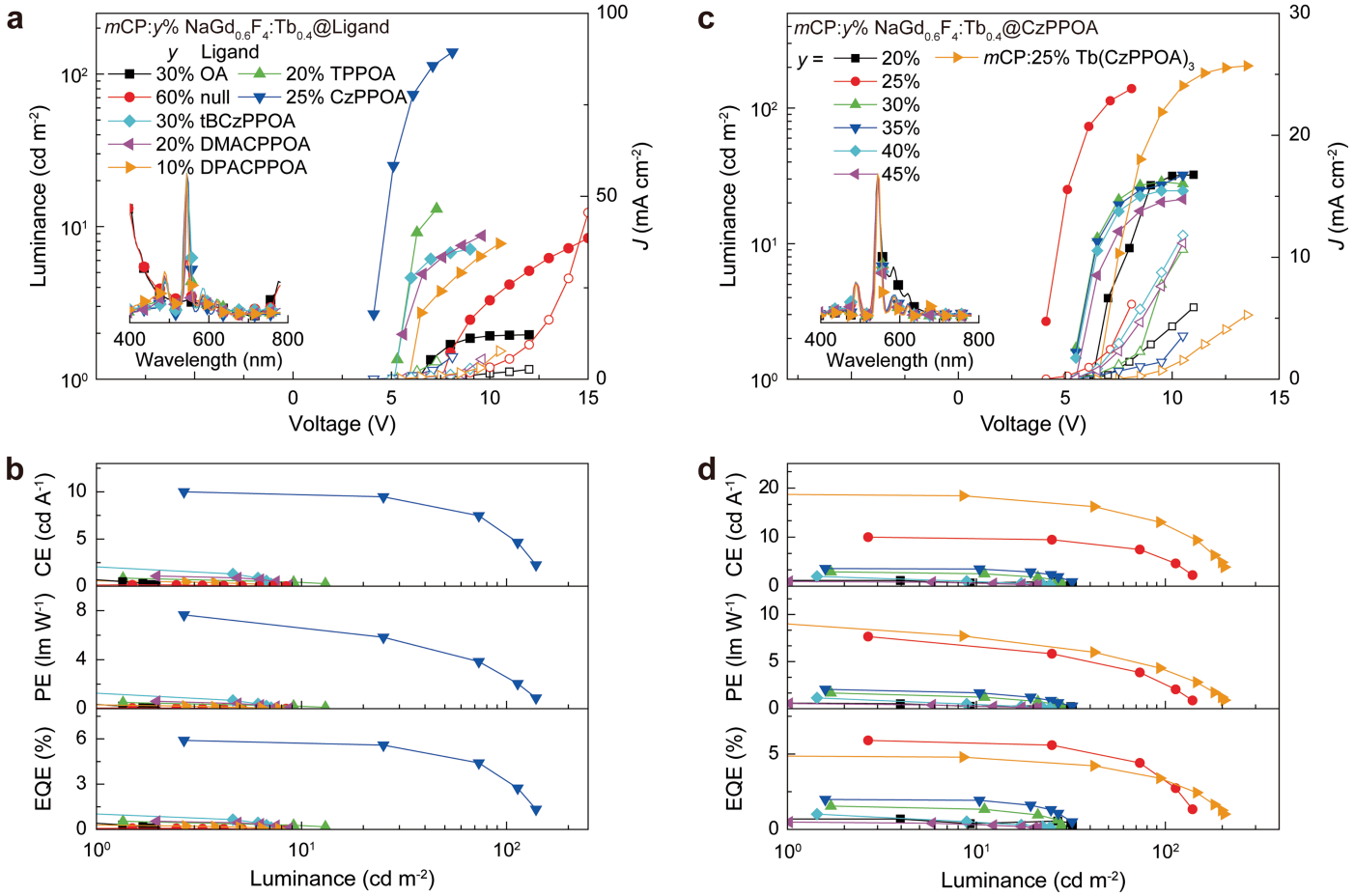

Extended Data Fig. 5 | EL performance of devices incorporating $NaGd_{0.6}F_4:Tb_{0.4}$ nanocrystals modified with various ArPPOA ligands and embedded in *m*CP films at different loading levels of CzPPOA. a, EL spectra (inset) and current density–voltage–luminance (*J*–*V*–*L*) characteristics of *m*CP:*y*%$NaGd_{0.6}F_4:Tb_{0.4}$@ligand at different *y* values. **b**, External quantum efficiency (EQE) versus luminance plots corresponding to the devices shown in **a**. **c**, EL spectra (inset) and *J*–*V*–*L* characteristics of *m*CP:*y*%$NaGd_{0.6}F_4:Tb_{0.4}$@CzPPOA devices at different *y* values compared with an *m*CP:25% $Tb(CzPPOA)_3$ molecular emitter control. **d**, EQE versus luminance plots corresponding to the devices shown in **c**.

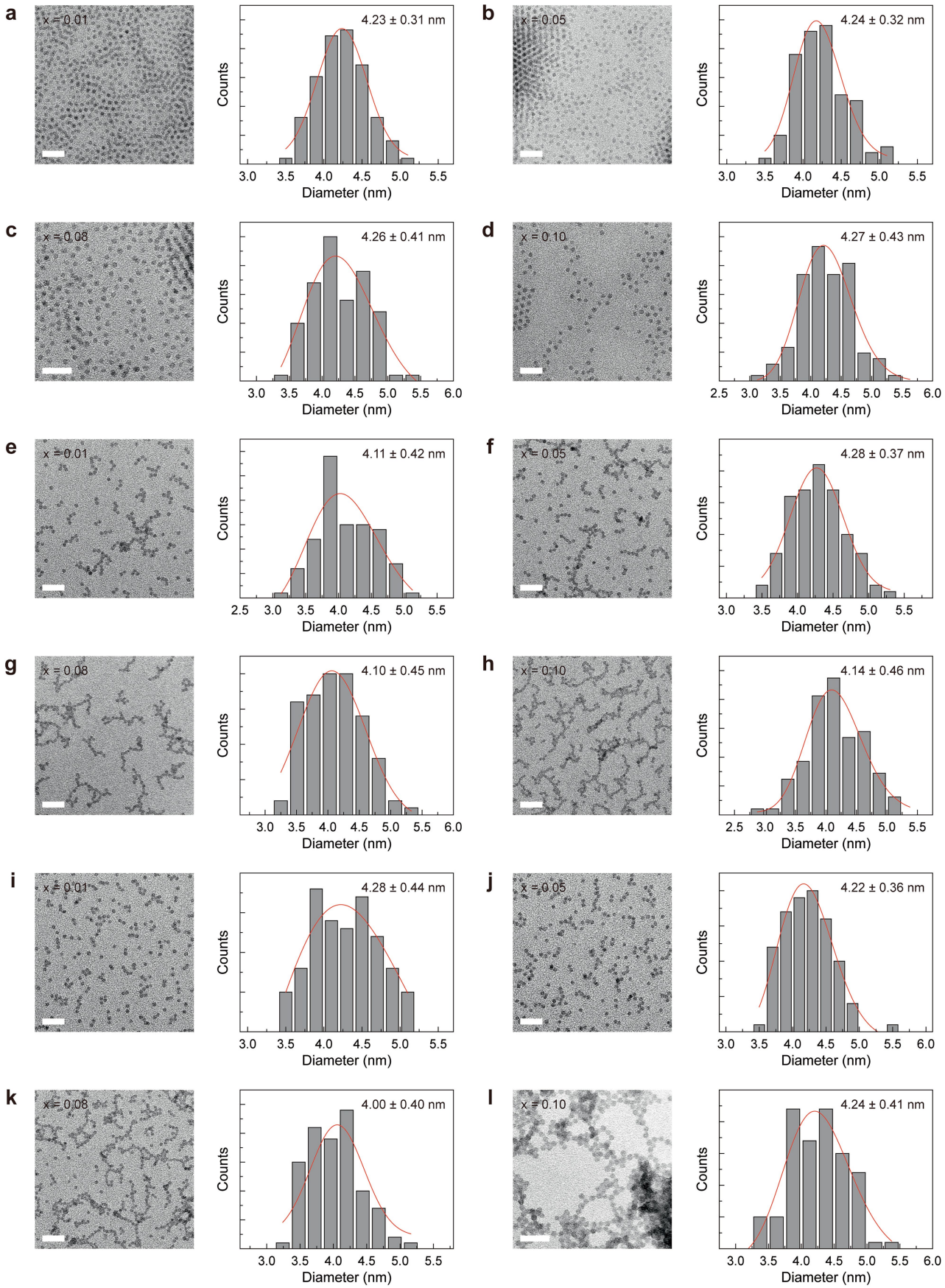

Extended Data Fig. 6 | Size distributions of $NaGd_{0.6}F_4$:$Tb_{0.4-x}Eu_x$ at varying Eu^{3+} doping levels. Transmission electron microscopy images and corresponding size distribution histograms of nanocrystals synthesized with different Eu^{3+} doping concentrations (x = 0.01, 0.05, 0.08, 0.10): $NaGd_{0.6}F_4$:$Tb_{0.4-x}Eu_x$@OA (OA-capped) (**a**–**d**); $NaGd_{0.6}F_4$:$Tb_{0.4-x}Eu_x$ (ligand-free) (**e**–**h**); $NaGd_{0.6}F_4$:$Tb_{0.4-x}Eu_x$@CzPPOA (functionalized with CzPPOA) (**i**–**l**). Scale bars, 20 nm.

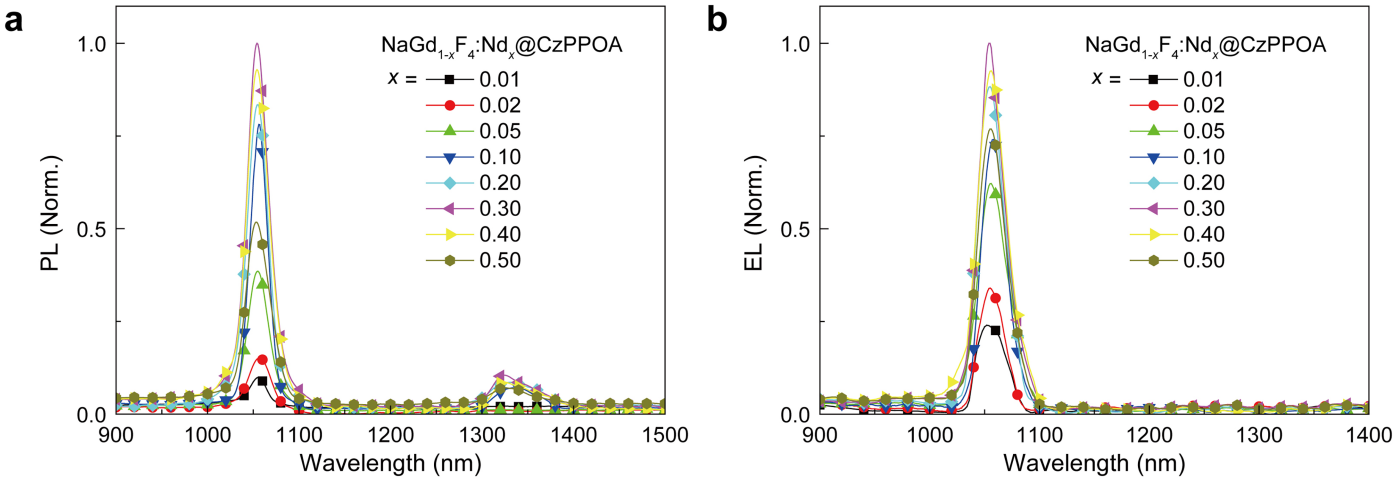

Extended Data Fig. 7 | The PL and EL spectra in the near-infrared region of $NaGd_{1-x}F_4:Nd_x$@CzPPOA nanohybrids. Steady-state PL (**a**) and EL (**b**) spectra for $NaGd_{1-x}F_4:Nd_x$@CzPPOA (x = 0.01–0.50).